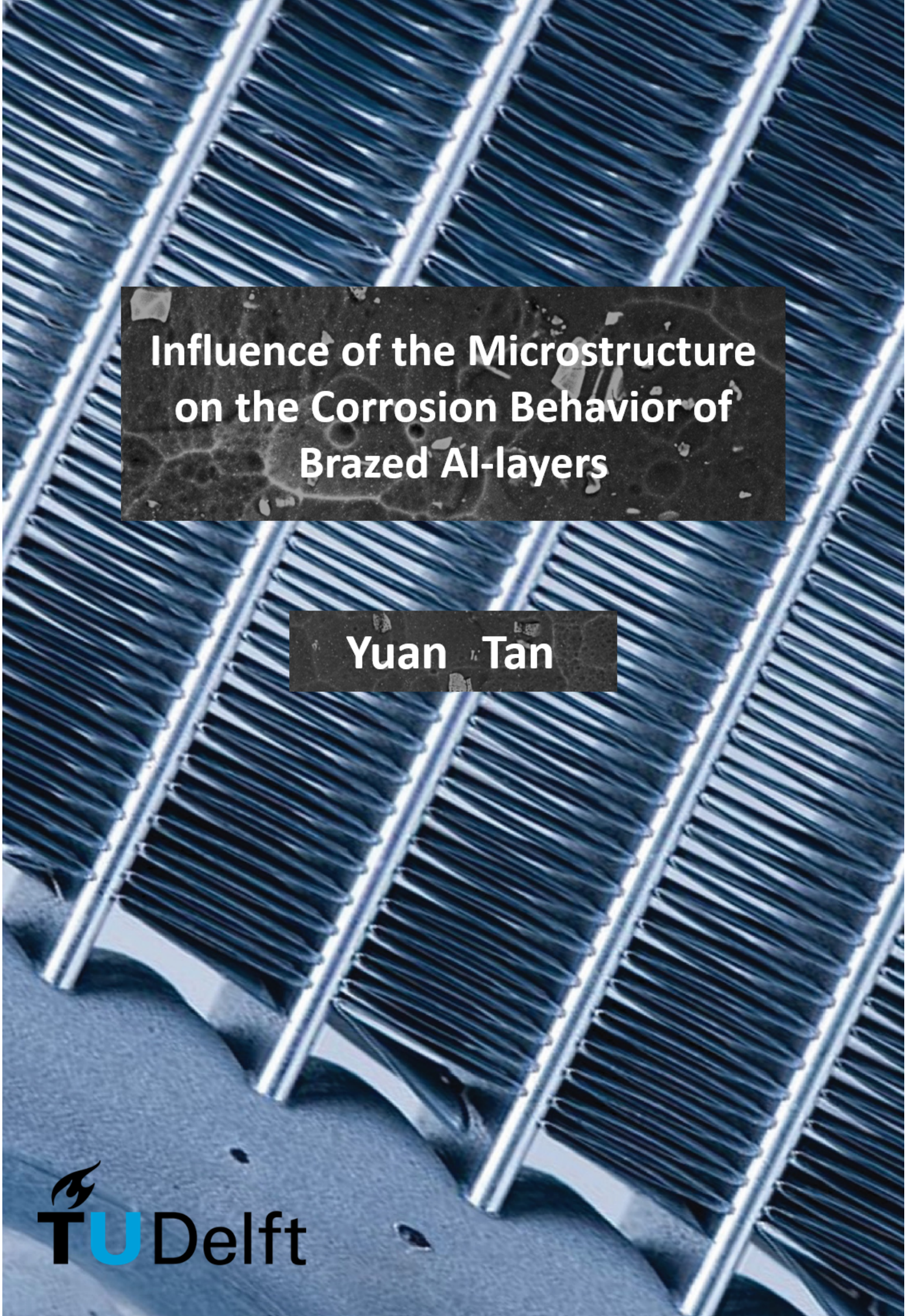
Influence of the Microstructure on the Corrosion Behavior of Brazed Al-layers
Yuan Tan
TU Delft

The cover page is from the website of ©2020 Norsk Hydro ASA
https://www.hydro.com/en-NO/industries/hvacr/micro-channel-heat-exchangers/

INFLUENCE OF THE MICROSTRUCTURE ON THE CORROSION BEHAVIOR OF BRAZED AL-LAYERS

Delft University of Technology

Master Thesis Report

Author:	Yuan Tan
Supervisor:	Dr. Yaiza Gonzalez-Garcia
Graduation committee:	Dr. Majid Sababi, *Gränges*
	Dr. Matthias Alfeld, TUdelft, MSE department
	Dr. Ursa Tiringer, TUdelft, MSE department

Materials Science and Engineering Department
Mechanical, Maritime and Materials Engineering Faculty

November 2020

TU Delft Delft University of Technology

Materials Science and Engineering

ABSTRACT

Aluminium alloy is widely used in the industry, while aluminium brazing sheets are mainly applied in heat-exchanger. The corrosion mechanism and corrosion behaviors have been studied in recent years. The aim of this thesis is to explore the difference of corrosion performance and microstructure at the distinguished regions in two specific systems - alloy FAB913 and alloy 8125.

The samples of two systems used for electrochemical measurements were etched to different depths by GDOES sputtering and covered by non-conductive tape with a 1 mm hole. The applied electrolyte is 0.05 M NaCl with 0.1 ml/L H_2O_2. Open circuit potential and electrodynamic polarization experiments were conducted at room temperature. The microstructure of the specimens before and after corrosion was observed under an optical microscope and scanning electron microscope (SEM). Scanning Kelvin probe force microscopy (SKPFM) characterization method was utilized to investigate the Volta potential variation through the cross-sections of two types of aluminium brazing sheets.

The results indicate that the re-solidified clad surface was susceptible to localized corrosion attack while the heat affected area and diffusion zone show good corrosion performance.

ACKNOWLEDGEMENTS

To finalize my graduation thesis, I have received a great deal of assistance and support .

Firstly, I am profoundly grateful to my supervisor **Dr. Yaiza Gonzalez-Garcia**, who gave me opportunity to take this project and patiently guided me to the end of the project. She gave me plenty of technical support and always encouraged me. And I would like to express my gratitude to **Dr. Majid Sababi**, who works for the company *Gränges*, providing me the experiment samples and a lot of helpful advice.

Secondly, my sincere thanks to all the friends I met in the lab, especially technician **Agnieszka Kooijman** and **Sander Van Asperen**. They gave me training and helped me all the time whenever I had difficulties with the experiments and devices.

Then, I would like to thank my parents, who give me mental and financial support to finish my master's degree. You are strict but open-minded, and you give me the power all the time to fight with all the uncertainties.

Last but not least, I would like to thank my Camelot family. You are always there for me. I can always get a hand whenever I have difficulties to overcome.

Again, thank you all!

CONTENTS

LIST OF FIGURES

LIST OF TABLES

ACRONYMS

1 INTRODUCTION

Aluminium alloy is one of the most popular materials widely used in the industry. In the past several decades, the application of aluminium alloy in heat-exchangers has been steadily increased, for example, in the automotive industry. Nowadays, the heat-exchangers mainly consist of aluminium brazing sheet. The aluminium brazing sheet is commonly made of two or three layers - one clad layer with one core layer or two clad layers with one core layer ("sandwich" structure). The typical clad layer is Al-Si alloy with lower melting temperature and the core layer is AA 3xxx series alloy. The life-time of the industrial products depends on the heat-exchangers' life-time, which is correlated with various properties of the Al brazing sheet. Therefore, it is vital to know the nature of the applied material.

This thesis report starts with a literature review following by the objective. Experiments were explained in Chapter 2, while the obtained results were discussed in Chapter 3. Then the report is finalized with a conclusion and recommendation.

1.1 LITERATURE STUDY

1.1.1 Aluminium Alloy

The strength of aluminum is its lightweight and resulting good formability. However, Al is too soft to be used for some engineering purposes, which restricts its variety of applications. To strengthen its mechanical properties, Al is always processed to alloy with other elements such as silicon, copper, manganese, magnesium, zinc, lithium, etc. Aluminium alloys are widely used in various applications due to their excellent properties after alloying with other elements. Eight Common aluminium alloy are listed in Table 1.1.

Aluminium Alloys Applied for Heat-exchanger

Applying aluminium brazing materials for heat exchanger in the automotive industries has been the trend since the 1990s [3]. Al alloys applying on heat exchangers are required for satisfactory strength, good thermal conductivity, and good corrosion resistance. Aluminium brazing sheet consisting of two series of Al alloys (AA 3xxx and AA 4xxx), which meets the requirements above, is commonly used for heat exchangers.

Table 1.1: A list of common Aluminium alloys [1, 2]

Alloying Elements	Alloy Series
Pure Alumium	AA 1xxx
Copper	AA 2xxx
Manganese	AA 3xxx
Silicon	AA 4xxx
Magnesium	AA 5xxx
Magnesium and Silicon	AA 6xxx
Zinc	AA 7xxx
Lithium	AA 8xxx

The main alloying element in the AA 3xxx series is manganese. Only a small amount of manganese (lower than 1.5 wt%) can be effectively added into aluminium [4]. AA 3xxx alloy has good corrosion resistance to an external severe environment, therefore, it is always called "long-life" alloy. Generally, AA 3xxx alloy functions as a core material in the aluminium brazing sheet supplying the necessary strength [2].

Silicon is added as the main alloying element in AA 4xxx alloys, decreasing the melting point of the alloy without producing brittleness. In the aluminium brazing sheet, this series of Al alloys are commonly used as the clad material out of the core material [2]. Sometimes, the brazed material shows a "sandwich" structure with two clad layers (AA 4xxx alloy) and a core layer in-between (AA 3xxx alloy). However, in this study, the brazing sheets consist of one clad layer and one core layer.

1.1.2 Brazing

Brazing is a joining process through which two or more materials are bonded with each other via capillary action [5]. Capillary action is explained as the ability of liquid flows in narrow spaces with the aid of external forces [6]. In the case of this study, it reflects that with the temperature increases, the clad material (also called filler material) melts, turns to liquids, and flows into the gap between the core metals (also known as parent material or base material). The clad material always has a lower melting temperature than the core material [7].

The brazing processes are always achieved in the controlled atmosphere brazing (CAB) furnace, where the atmosphere is normally dry and inert nitrogen. The brazing temperature is commonly close to the liquidus temperature of the clad material and below the melting temperature of the core material [3]. The reason for the application of CAB in the industry is that this brazing technique can be done at atmospheric pressure continuously and is required relatively low investments and maintenance costs [8].

Diffusion after brazing

During the brazing process, the clad material partly alloys with the core metal. The metal atoms from both metals move oppositely and penetrate into the other metal. This process is called diffusion (Figure 1.1). And the region with a diffusion concentration profile is called the diffusion zone.

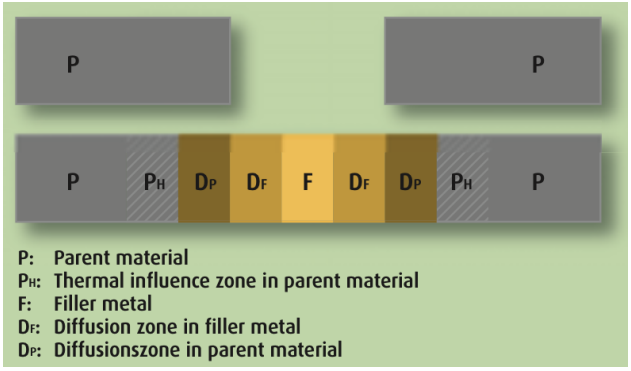

Figure 1.1: A schematic diagram of diffusion process during brazing [9].

After brazing, the metal atoms in the clad material can be detected in the core metal, vice versa, the atoms from the core metal can be found in the clad material as well. The formation of the diffusion zone is dependent on the brazing temperature and time. Not all these layers in Figure 1.1 would exist. If the brazing time is long enough or the brazing temperature is high enough, then the layer of filler metal F may disappear [9].

1.1.3 Effect of Brazing Process on microstructure of Aluminium Brazing Sheet

Brazing process of aluminium sheet is often conducted in a CAB furnace, details are mentioned in Section 1.1.2. The material is then heated up following a standard CAB brazing cycle [3]. For instance, Afshar selected the holding temperature as 600 ^{0}C which is close to the liquidus temperature of the clad material and the cooling rate as 60 ^{0}C/min [10].

The brazing process can cause microstructural variations of aluminium alloys, depending on many factors, such as brazing temperature and time. The microstructural evolution of the brazing sheets can be investigated via observation of surface and cross-section, which is easily can be achieved by optical microscope (OM) and scanning electron microscope (SEM). In addition, Elemental evolution can be analyzed by electron probe X-ray micro analysis (EPMA). Through energy dispersive X-Ray spectroscopy (EDS), particles at the surface and bulk material can be identified, as well as the element distribution map.

Microstructure in Non-brazed and Brazed Aluminium sheet

Before being brazed, there are Si phases (in dark grey) and precipitates rich in Mn and Fe can be observed in the clad layer and, respectively, which is obviously shown in Figure 1.2 (a) [3]. This corresponds to the results obtained by Afshar

[11]. The elongated coarse particles presented in the clad material are Si particles and as well as some small precipitates with Al, Fe, Cu, and Si elements. More types of precipitates with different compositions and sizes existed in the core material with two main distinguished sizes. One of them is α-Al(FeMn)Si and the other are mainly α-Al(FeMn)Si and Al_2Cu particles. It is worth mentioning that all the copper-containing particles are small particles with a size less than 1 μm. In the non-brazed clad layer, the existing major particles are β-AlFeSi and α-Al(FeMn)Si. Moreover, the precipitates in the clad layer contain less amount of Cu than those in the core layer. As for the surface of the non-brazed sheet, the precipitates homogeneously distribute in the Al-matrix referring to Figure 1.2 (c).

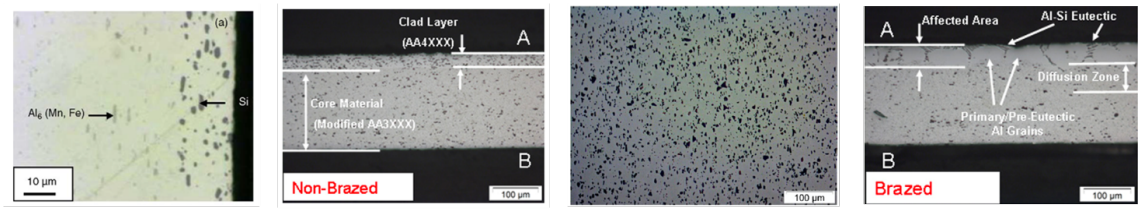

Figure 1.2: Optical images of: (a) cross-section of non-brazed sheets [3]; (b) cross-section of non-brazed sheets; (c) the surface of non-brazed sheets; (d) cross-section of brazed sheets [11].

After brazing, both the microstructure of the clad layer and core material has been changed. A grain boundary penetration scheme is activated during the brazing process. A liquid layer forms at the interface between the clad and the core material. It progresses into the core alloy as a film when brazing the clad layer on the core layer [12]. This partly explains the reason for the microstructural evolution. Schmatz also mentioned that in AA 3xxx alloys, the penetration was restricted by the presence of stable particles containing manganese - Al_6Mn in the core layer.

A region that exists after brazing is called heat affected area (HAZ), as shown in (Figure 1.2 (d)). The density of the precipitates is low in this area due to the element diffusion. It was observed that the Al-Si eutectic phase accumulated at the surface and in between the primary/pre-eutectic Al grains. It is a mixed structure of Si and α-Al, where the α-Al is different from the primary α-Al because all the elements concentrate in the eutectic areas. A diffusion zone was defined by the Si diffusion path since the Si element has the highest diffusion capability diffusing into the core material. According to some research, a band of dense precipitates (BDP) would form at the interface between the clad and core material during the brazing process. The BDP in the aluminium brazed sheets is commonly located in the diffusion zone and filled with α-Al(FeMn)Si particles [13, 8, 14].

With the implantation of the EDS, the elemental distribution mapping technique was utilized by the researchers. Compared with the microstructure of the sheet

before brazing, the major differences after brazing are the decrease of the Cu content in the particles and the increase of Si concentration in the diffusion layer. Cu-rich points occurred on the surface of some large particles. Cu accumulated in Al-Si eutectic phase at the surface and in the "affected area" (Al-Si phase). The high solubility and high diffusivity of Cu in the liquid Al matrix were assumed to be the appropriate explanation of this consequence.

The dominant particles in the core layer of the aluminium brazed sheet are α-Al(FeMn)Si, Al_6Mn, and Al_2Cu while the major phase in the clad material is Si particles (β-AlFeSi is the second dominant particle). In the diffusion region, the species of particles are almost the same comparing with the particles in the core material, except for Al_6Mn [7, 10, 11].

Effect of Brazing Process on Corrosion Mechanism in Aluminium Alloys

Depending on different properties relating to compositions and the external environment, various corrosion mechanisms will be activated. It is known that uniform corrosion is the common corrosion mechanism occurring in pure aluminium and some non-brazed aluminium alloys, contributing to evenly distributed deposition or corrosion products over the whole exposed surface after the attack. A case of uniform corrosion in a non-brazed aluminium sheet is indicated in Figure 1.3. Due to the relatively low reaction rate and predictability, uniform corrosion is considered as the least dislikable corrosion type to aluminium alloys [15, 16].

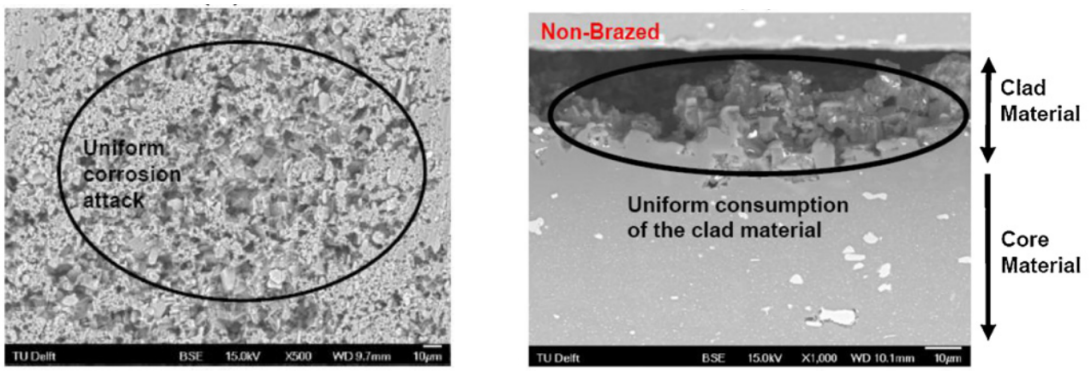

Figure 1.3: SEM images of non-brazed Al alloy under uniform corrosion: (a) surface (b) cross-section.[7]

However, two dominant corrosion mechanisms in aluminium brazing sheet are: pitting corrosion and intergranular corrosion (IGC)) [17].

Pitting Corrosion

Pitting is a type of corrosion attack which is dangerous because of its non-detectability. It is a localized attack and contributes to Al-matrix dissolution, forming pits that may be covered by the corrosion products. In most cases, any non-uniformities, inclusions, or defects at the sample surface can be a starting

point of pitting corrosion in a homogeneous environment. If the sample is defect-free and placed in an aggressive environment containing chloride ions, pitting would initiate at the oxide destroyed spots due to the damage of chloride ions to the passive film [18, 19]. It was found that the concentration of chloride ions tends to influence the severity of pitting corrosion [16, 20, 21].

Basically, pitting corrosion is considered as self-catalytic mechanisms, which can be divided into two processes: the pit generation process and its depth growth process. Once a pit starts to grow, the developed condition promotes further pit growth. Due to hydrolysis process ($Al^{3+} + 2H_2O \Longleftrightarrow Al(OH)_3 + 3H^+$), the pH value inside the pits will decrease after pits generate. Thus the pits tend to further propagate into the bulk material in an aggressive environment [22].

As for aluminium brazing sheet, defects at the surface such as second phase precipitates can easily be the starting point of destruction under an aggressive environment.

Intergranular Corrosion (IGC)

IGC is another form of corrosion attack which is influenced by microstructure. The corrosion happens because of the electrochemical difference between the grain boundary and the bulk or adjacent regions, which means the boundaries of the material are more susceptible than the other parts. The grain boundary region becomes an anode while the inner grain acts as a cathode. A galvanic cell, therefore, forms with a large cathode and a small anode under the electrochemical potential difference which will lead to rapid corrosion at the anode (grain boundary). IGC may initiate at a pit as pitting corrosion, but it differs from pitting corrosion with a faster propagation rate. After IGC activation, it propagates along the grain boundaries so that continuous boundaries corresponding to high susceptibility to IGC [21]. The spread of IGC may finally result in exfoliation corrosion [13]. Figure 1.4 shows the intergranular corrosion propagation in an AA 4045/3004/4045 brazing sheet.

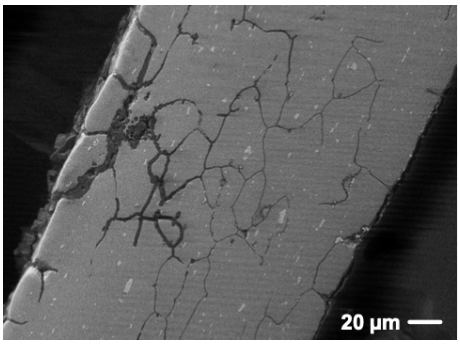

Figure 1.4: Propagation of Intergranular corrosion in AA 4045/3003/4045 brazing sheet alloy (an image of cross-seciton) [17].

Corrosion Mechanisms in Aluminium Brazing Alloys

The corrosion attack of a brazed sheet at the surface is more severe and less uniformly than that of a non-brazed sheet. For the brazed Al sheet, the non-uniform localized corrosion is the dominant mechanism of the attack, specifically is IGC. It is known that IGC has two forms in Al alloys [23]. One is crystallographic IGC, which is controlled by recrystallization. Corrosion-sensitive regions form at high-angle boundaries of the recrystallized grains. Void accumulation and coagulation is the possible reason for this type of IGC. The other one is structure-decomposition IGC. Corrosion-sensitive regions form near the incoherent or partly coherent phase particles at the grain boundaries. Preferential corrosion attack then occurs at the grain boundary zones where the necessary elements with corrosion resistance are lost.

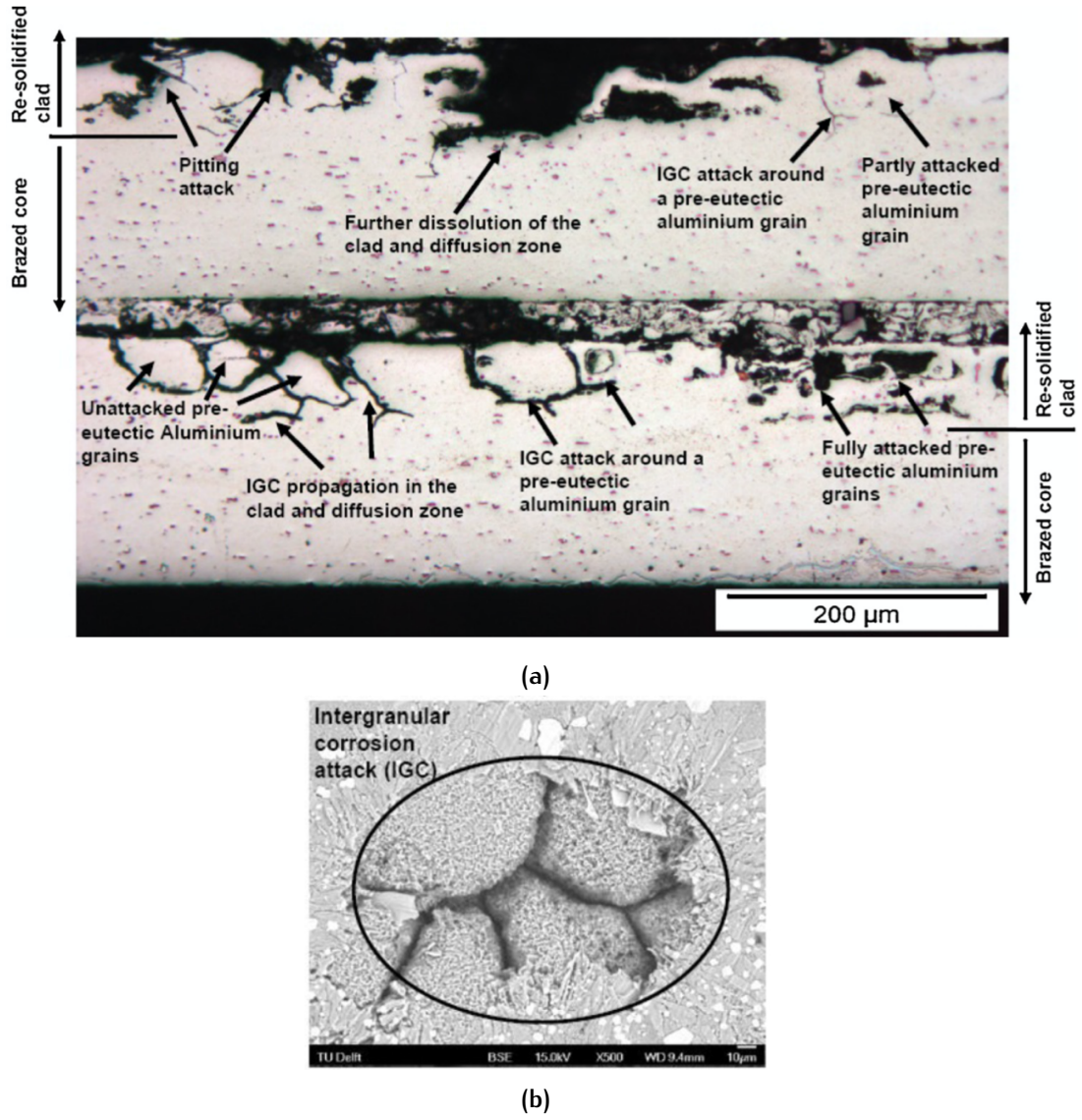

Figure 1.5: (a) Optical images of cross-section of corroded Aluminium brazing sheet [11]; (b) SEM images of IGC corrosion [7].

As mentioned in the previous section, intermetallic particles form at the grain

boundaries such as α-Al(FeMn)Si and Al_2Cu, and Cu accumulates at the eutectic phases in the resolidified clad material during brazing. These leads to IGC susceptibility. In Afshar's research, it is shown that (Figure 1.5) the pitting corrosion initiates at the Al-Si eutectic phases because the eutectic phases have a low pitting potential than the primary α-Al phases. When the intermetallic particles exist in the eutectic phases, they provide cathodic activity and function as the initiation sites of the corrosion attack when exposed to a corrosive environment. Intermetallic particles draw down the nobility of the matrix. So the eutectic phases with intermetallic particles and continuous grain boundaries are expected to be the early failure spots in the resolidified clad material. IGC happened preferentially at the boundaries around the eutectic grains and propagated along these grain boundaries in the clad material and diffusion zone.

After brazing, the eutectic phase appears at the surface of the re-solidified clad material and among the primary α-Al grains, which becomes the weakest area to localized corrosion attack. Since Si is nobler than the eutectic phases, the latter one will act as an anode in a corrosive environment. Due to the extremely low solubility of elements in the Si phase, the Si phase is considered as the one with the smallest change before and after the brazing process. Thus it is used as a reliable reference for measuring Volta potentials. Afshar applied SKPFM to measure the local Volta potential value to compare the corrosion properties before and after brazing due to the complex varying localized microstructure. Clad material has the sacrificial capability to protect the core material inside due to the potential difference before brazing. After brazing, changes in microstructure accounts for the decrease of the potential difference between resolidified clad material and core material. This is expected to lower the protection capability of clad material to the core. From this perspective, brazing weakens the corrosion resistance of the sheet. Confirmed by researchers (Figure 1.5b), the eutectic regions formed among grain boundaries are the priority attack points. The resolidified clad material has a high susceptibility to the localized corrosion and the corrosion attack develops further into the core material, which means the brazed clad material cannot provide sufficient protection for the core material [7].

In Afshar's research, he found that both brazed and non-brazed core materials have similar anodic polarization responses. They are susceptible to the localized corrosion attack due to the dramatic rise in current density at the potential close to the corrosion potential value in the anodic polarization curves. As for cathodic polarization, the dissolution of some particles such as Al_2Cu and enrichment of the core material with alloying elements account for the low reactivity cathodic polarization responses of the brazed core material.

Other researchers such as Z. Yuan found that the formation of BDP enhances the corrosion property to some extent. There are many α-Al(FeMn)Si precipitates in BDP, which show low corrosion potential when the corrosion spread to BDP. Due to the high density of α-Al(FeMn)Si particles, the corrosion mechanism is replaced by exfoliation corrosion (Figure 1.6). After the clad material

being corroded, the core material is the next. Pitting corrosion proceeds in all directions, causing fast perforation of the Al brazing sheets. The existence of BDP largely improves the corrosion lifetime of the Al brazing sheet and prolongs the perforation time [13].

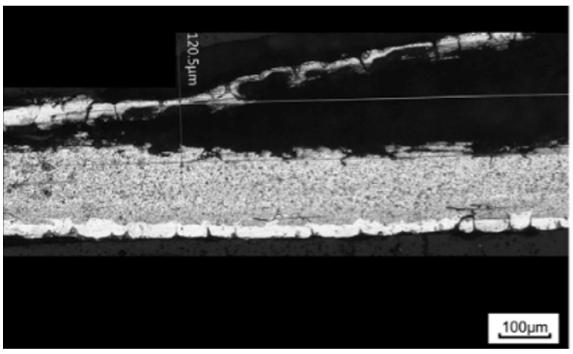

Figure 1.6: A case of corrosion mechanism replaced by exfoliation [13].

1.2 OBJECTIVE OF THIS THESIS STUDY

Electrochemical properties of the brazed aluminium alloy at the re-solidified surface of the clad layer and through the cross-section has been extensively investigated. The study combining GDOES depth profiling and electrochemical measurement is limited.

In this thesis, two systems of brazed Al alloy were studied: alloy FAB913 and alloy 8125. The main difference between the two materials is the concentration of Mn, Cu, Fe, and Si alloy elements in the core layer. The addition of Cu, the amount of Si, and the Mn/Fe ratio have been proved to be the critical factors that can influence the mechanical and corrosion properties. This thesis aims to investigate the electrochemical response in different depths of the brazing sheet (from the re-solidified clad to the core layer) and the microstructural evolution after corrosion. Besides, to discuss the feasibility and practicality of using GDOES etching craters for conducting electrochemical experiments.

The specimens were etched to different depths by GDOES sputtering. Open circuit potential and potentiodynamic polarization measurement were displaced in the GDOES etching craters to study the anodic and cathodic reaction behavior in different depths. Moreover, comparing to the GDOES depth profiling result to discuss the reason for those electrochemical responses. The optical and scanning electron microscope was used to investigate the surface morphology before and after polarization and detect intermetallic particles at each depth. Also, scanning Kelvin probe force microscopy technology was applied to obtain the Volta potential variation through the cross-section.

2 EXPERIMENTS

In this research, the corrosion behaviors of samples are investigated through electrochemical tests in the electrolyte with specific concentration. Applied techniques, experiment materials, and experimental parameters are indicated below. In addition, it is vital to control the concentration of the electrolyte to make sure the corroded surface would be suitable to be observed (The details will be discussed in Section 2.4).

2.1 EXPERIMENT MATERIALS

All the samples were provided by *Gränges*. Both two types of samples are formed by two layers (core layer and clad layer). Core and clad layers are 3xxx and 4xxx aluminium alloys, in which the main alloying elements are manganese (Mn) and silicon (Si), respectively. Their chemical composition of the alloys is indicated in Table 2.1. Two clad layers have similar elemental content, while the core layers have slight differences with composition.

The aluminium alloys were manufactured through direct chill (DC) casting. The brazed aluminium sheets were heated up to 525°C and kept at that temperature for 10 hours. After heat treatment, they were rolled from the thickness 3.7 mm to 0.85 mm and at last to 0.27 mm.

Table 2.1: The chemical composition of commercial sample P14-00913 and P18-00555.

Sample	Alloy	Chemical composition							
		Si	Fe	Cu	Mn	Mg	Zr	Ti	Al
P14-00913 (FAB913)	FA7929 (core)	0.52	0.27	0.53	1.4	0.01	0.01	0.14	Bal.
	AA4343 (clad)	10.0	0.19	0.01	0.02	0.02	0.01	0.01	Bal.
P18-00555 (8125)	FA7873 (core)	0.05	0.15	0.80	1.65	0.01	0.10	0.05	Bal.
	FA6690 (clad)	10.0	0.19	0.01	0.01	0.01	0.01	0.01	Bal.

2.2 EXPERIMENT TECHNIQUES

2.2.1 GDOES Etching

The brazed samples were etched to different depths by glow discharge optical emission spectroscopy (GDOES) sputtering. The diameter of the GDOES crater was around 3.5 mm. A GDOES depth profiling analysis was done to show the variation of the distribution of the alloying elements. The element distribution profile contributed to explaining the electrochemical responses of brazed samples at different depths. The crater obtained by GDOES sputtering is shown below in Figure 2.1.

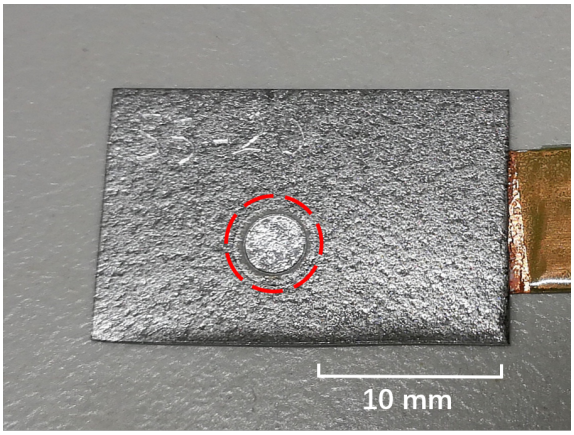

Figure 2.1: A picture of GDOES crater.

2.2.2 Microscopical Observation

In this research, optical microscopy and scanning electron microscope were utilized to investigate the topography and morphology of the sample surface before and after polarization experiments, which is a vital part of the experiment to obtain a relationship between electrochemical responses and microstructural evolution.

Scanning Electron Microscope (SEM)

The SEM uses a beam of focused electrons with high energy to acquire images. The information that can be obtained from the sample is shown in Figure 2.2a. When the electron beam encounters the sample surface, an interaction volume is generated (Figure 2.2b). The size of the interaction volume is closely rated to the energy of the incident electron beam. The higher the energy of the electron beam, the larger the size of the interaction volume[24].
Both of secondary electrons (SE) and back-scattered electrons (BSE) are two commonly used signals for observing samples produced by electron-sample interactions. SE are detected to observe the topography of the sample surface. BSE are mainly used to detect the contrast of the areas with different chemical compositions. EDS, in conjunction with SEM is used to analyze the chemical composition

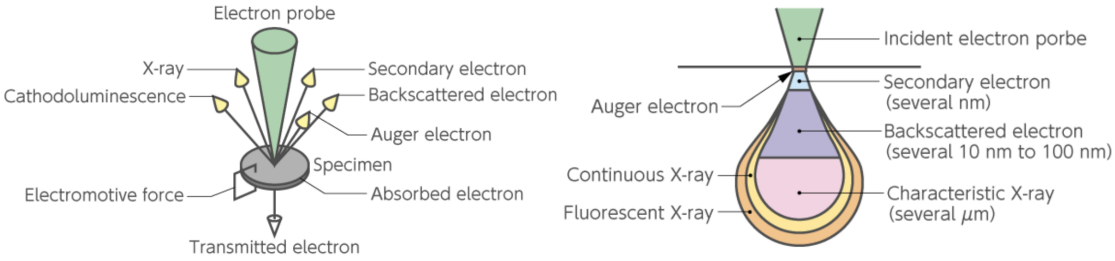

Figure 2.2: Schematic diagrams of (a) Information can be obtained from the sample. (b) Interaction volume of electron beam with sample. (From the website of JOEL)

in the test area by detecting and collecting the X-rays emitted from the sample after bombarded by the electron beam.

The type of optical microscope used for this research is Leica DM LM; the applied magnitude is 10x. JSM-IT 100 table-top SEM and JOEL EDS system were used for microstructural observing and element analysis. The images and chemical composition analysis data were collected with an accelerating electron volt of 15 kV.

2.2.3 Electrochemical Measurements

Electrochemical measurements are necessary for investigating the corrosion behavior of samples. The following two methods were used in this thesis project and the results are discussed in Chapter 3: open circuit potential (OCP) and Tafel polarization (TP). The electrochemical experiments are all performed in the aqueous environment, the concentration of the solution used for the experiments was determined under trials (Section 2.4). More details about experiment parameters are indicated in Section 2.3.

Open Circuit Potential (OCP)

OCP is measured when the electrochemical cell is disconnected to the power amplifier; in other words, there is no current and no potential is applied to the working electrode. The OCP measurement is usually operated as a pre-procedure to monitor the system state. The system is normally required to reach a thermodynamically equilibrium state before further measurements. When the potential variation is independent of time, it means that the equilibrium state is reached.

Tafel Plot extrapolation (TP)

Tafel extrapolation is a widely-use method to determine the corrosion current density i_{corr}, which is expressed in terms of the current per unit area of the working electrode. From the corrosion current density, the corrosion rate can always be calculated. The reaction rate is mainly controlled by two types of kinetic phenomena. One of them is charge transfer. The driving force during

polarization is the overpotential (η). As the driving force increases, the reaction rate increases as well. The other mechanism is mass transfer. Under this circumstance, mass transfer through the electrolyte to the surface of the working electrode controls the reaction rate. The current density is related to the concentration and diffusivity of the species of interest in the solution. Once the reaction rate has reached a limiting value, further increase in driving force will function no more [25].

The polarization curve is obtained by the anodic and cathodic potentiodynamic scan. A complete idealized polarization is sketched above (Figure 2.3). In a real case, some or all of these characteristics may be present.

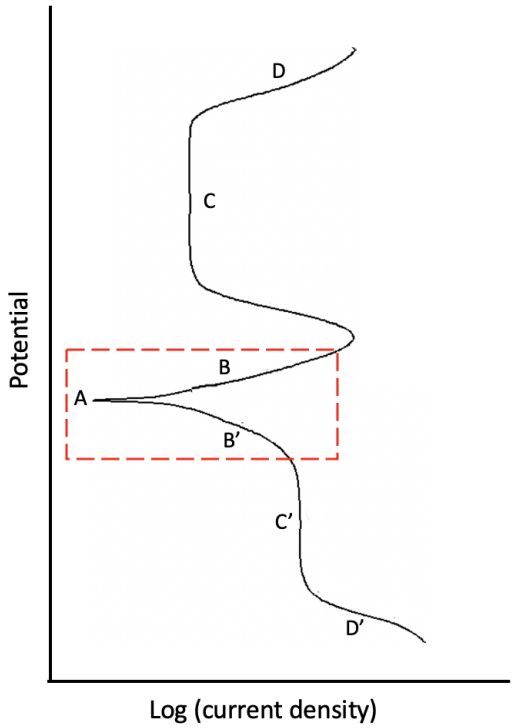

Figure 2.3: A schematic diagram of ideal polarization curve [25].

The OCP is located at point A. At this point, the net rate of anodic and cathodic reaction on the electrode surface is zero. The upper part of the curve is the anodic polarization branch, while the lower part is the cathodic polarization branch. Region B, C, and D represent the active, passive, and transpassive regions, respectively. In the active region, metal dissolution is the dominant reaction, releasing metal ions and electrons. Region B′ represents the oxygen reduction reaction. In region C′, a limiting current density has reached, and a further decrease in the applied potential contributes to rare variation in reaction rate. If the potential keeps decreasing, here comes another cathodic reaction in region D′, which can be hydrogen evolution (also known as water reduction reaction.

This thesis report focuses on the red-dotted region in Figure 2.3, which is the specific region that Tafel extrapolation method can be applied (the detailed curve is indicated in Figure 2.4). The metal specimen is always polarized from -300

mV to +300 mV with respect to the open circuit potential to conduct the Tafel polarization curve [26].

In the case of aluminium alloy, the aluminium alloy dissolves and resulting in

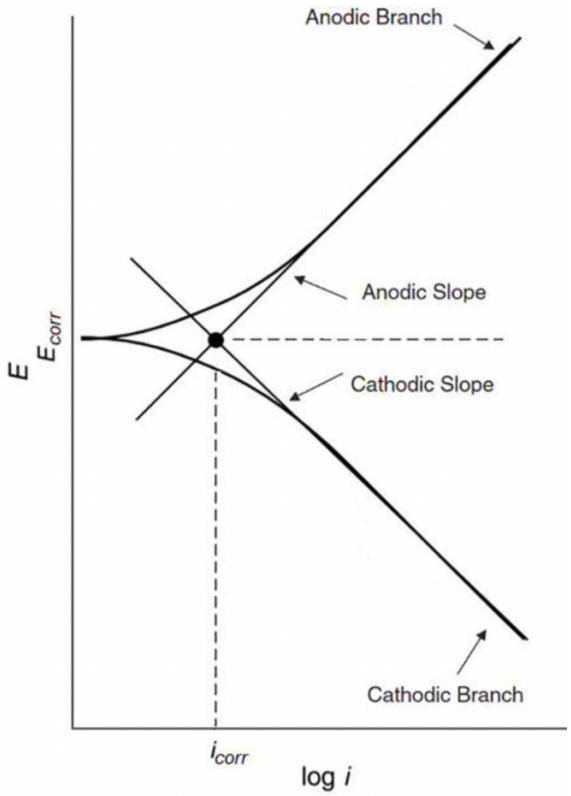

Figure 2.4: A schematic diagram of Tafel curve and extrapolation [27].

the generation of electrons during anodic polarization (the upper branch): Al $\longrightarrow Al^{3+} + 3\ e^-$. During cathodic polarization (the lower branch), the dissolved oxygen is consumed: $O_2 + 4\ H^+ + 4\ e^- \longrightarrow 2\ H_2O$.

The extrapolation of the linear portion of two branches is utilized to gain the corrosion current density and potential. The slopes of two extrapolation lines are the anodic and cathodic slope. The intersection of two lines indicates the corrosion potential (E_{corr}) and corrosion current density (i_{corr}). At this point, the rate of cathodic reaction is equal to the rate of anodic reaction, which means the net current flow is zero at the electrode.

The relationship between the overpotential (η) and the current density (i) at this Tafel polarization region is given by Tafel [26]:

$$\eta = a \pm b\, log(i) \tag{2.1}$$

where a is a constant, b is the Tafel slope of the anodic or cathodic reaction.

In some cases, the diffusion rate of oxygen in the solution influences the shape of the cathodic curve. This situation is indicated in Figure 2.5. The cathodic

branch represents the oxygen reduction reaction. The reaction is limited by how fast and how much the oxygen may diffuse to the surface of the working electrode. When the dissolved oxygen is not enough for the reduction reaction, the cathodic current density would be limited. This is a normal case that the electrochemical dissolution of aluminium alloy is controlled by the diffusion [28].

Due to the small anodic Tafel slope and large cathodic Tafel slope, it is not easy to find a pure Tafel region. Therefore, Tafel extrapolation method is hardly helpful as a limiting current has reached, which can lead to erroneous conclusions. Corrosion current densities and corrosion potentials were defined by Tafel

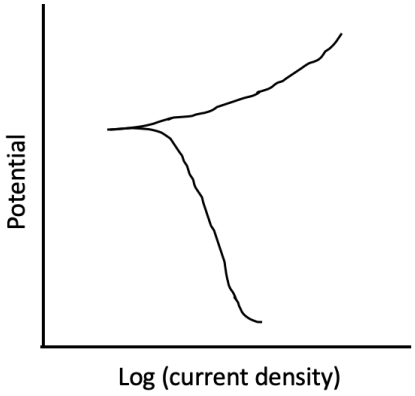

Figure 2.5: A schematic diagram of the case of diffusion limitation.

extrapolation via a built-in software of EC-lab (Tafel fit).

2.2.4 Scanning Kelvin Probe Force Microscope (SKPFM)

Scanning Kelvin probe force microscopy (SKPFM) is widely used to investigate the corrosion mechanism in aluminium alloys various intermetallic particles[29], which is based on the measured Volta potential. Volta potential is a material property that can demonstrate the thermodynamic propensity of a metal to have electrochemical reactions[30]. In this thesis, the Volta potential is helpful in defining the cathodic and anodic sites in the aluminium alloy matrix.

The basic working principle of SKPFM is similar to atomic force microscopy. An alternating current is applied to the probe or sample, generating electrostatic force between the sample and probe. A compensating potential is then needed to balance that electrostatic force, which is known as Volta potential difference. The result is highly dependent on the surface condition and environment[31].

The SKPFM experiment did for this thesis is to characterize the Volta potential variation at the cross-section of two types of samples. The experiment was placed in an open-air environment with ambient temperature and humidity. The cross-sections of samples were cold mounted in a non-conductive resin and ground by sandpaper in a sequence of 320, 800, 1200, 2000, and 4000 (grid number), then polished with 3 and 1 μm polishing cloth.

2.3 EXPERIMENTAL SET-UP AND PARAMETERS

All the electrochemical measurements are performed under the aqueous environment. A three-electrode setup is used during the experiments, consisting of a stainless steel mesh as the counter electrode, a silver chloride (Ag/AgCl) as the reference electrode, and a aluminium alloy sample as the working electrode. The schematic diagram of the experimental setup is shown in Figure 2.6.

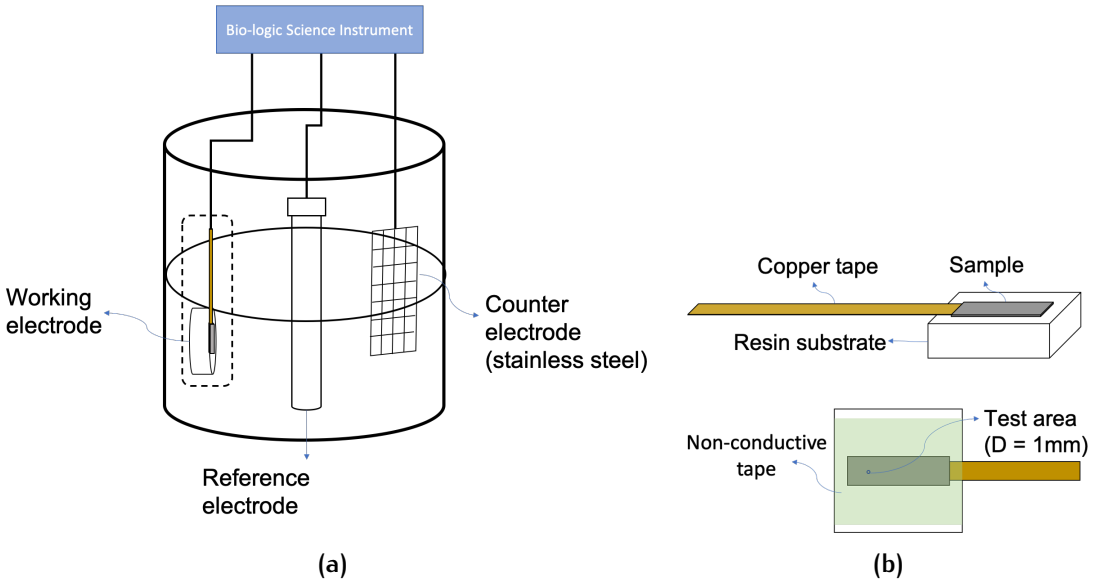

Figure 2.6: Schematic diagrams of (a) Experimental setup. (b) detailed information of the dashed area in (a).

Since the sample is too thin, it was placed on a substrate made of resin and fixed by non-conductive tape. A piece of copper tape was connected to the sample and functioned as an electrical wire during the electrochemical tests. A hole was left on the non-conductive tape. The surface exposed under the tape is the test area. The test area is a circle with a diameter of 1 mm. The tests were done at the surface and as well as in the GDOES craters with different depths to gain the electrochemical responses as a function of crater depth.

Figure 2.7: A picture of prepared sample.

The workstation of VSP-300 of Bio-logical Science instruments was used to finish the electrochemical measurements. Polarization experiments started after around 10 mins of potential stabilization. The applied potential was set with

respect to OCP, ranged from -200 mV vs. OCP to +200 mV vs. OCP. More details of setup are directly shown in Figure 2.8 and Figure 2.9.

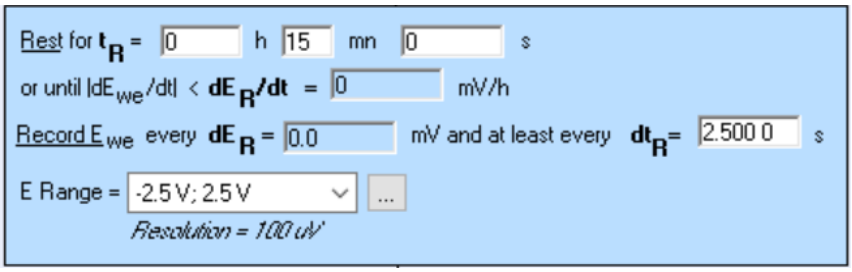

Figure 2.8: Software setup of OCP.

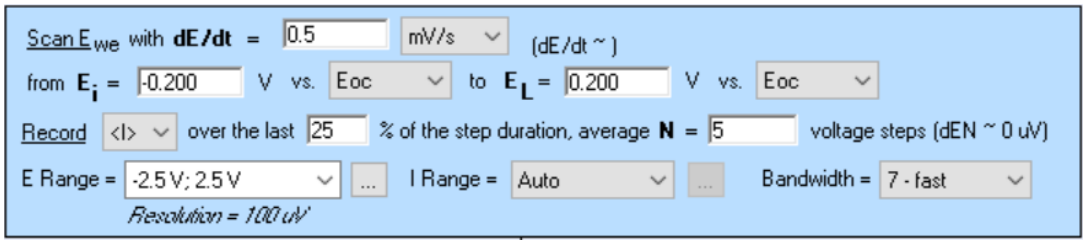

Figure 2.9: Software setup of TP.

2.4 SELECTION OF THE ELECTROLYTE

The electrolyte needs to be neither too aggressive to make the sample surface over-corroded nor too slight that no obvious features can be observed. Therefore, a concentration of NaCl solution - 0.05 M was selected after several trials.

However, the OCP curve obtained in the solution 0.05 M NaCl vibrated a lot as shown in Figure 2.10. To make the curve more stable and less noise, H_2O_2 was added. It took less time for the system to get an equilibrium state with the addition of H_2O_2 and the strong vibration disappeared.
The introduction of H_2O_2 changed the reaction that happened on the cathode. The cathodic reaction switched from oxygen reduction to hydrogen peroxide reduction, and the latter one is easier to initiate: $H_2O_2 + 2\,H^+ + 2\,e^- \longrightarrow 2\,H_2O$.

It decreased the cathodic polarization and accelerated the corrosion to some extent. The OCP is slightly higher in the solution containing H_2O_2, which is likely due to the increased cathodic current. Since the results of OCP was significantly optimized by adding H_2O_2, all the electrochemical measurements were conducted in solution containing 0.05 M NaCl + 0.5 ml/L H_2O_2.

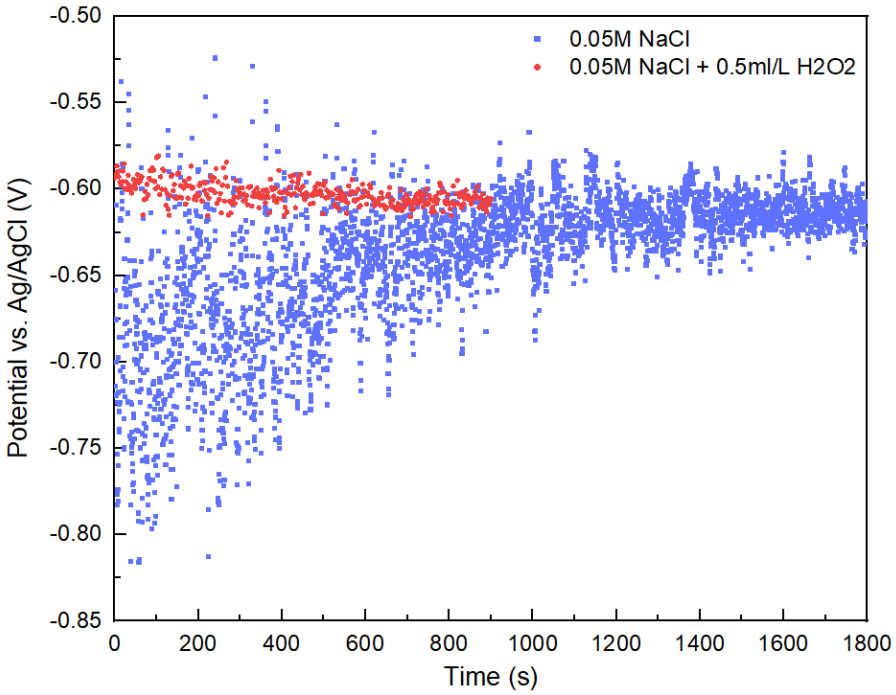

Figure 2.10: The comparison of OCP curves when test were placed in solution 0.05 M NaCl with/without H_2O_2.

3 RESULTS AND DISCUSSION

In this chapter, two systems of aluminium alloy FAB913 and 8125 were evaluated by the electrochemical response in the electrolyte 0.05M NaCl solution with 0.1 ml/L H_2O_2 combining with the microstructural investigation. OCP measurement was conducted prior to the polarization experiment. The GDOES elemental concentration variation profiling corresponds to the result of polarization. Optical microscope and SEM were applied before and after electrochemical measurement to explore the microstructural evolution in the brazed Al alloy. At last, SKPFM was used to investigate the Volta potential variation through the cross-section.

3.1 SYSTEM FAB913

3.1.1 Microstructural Analysis

The microstructure of the aluminium sheet has significantly changed after brazing, through which optical images of the cross-section of the material FAB913 before and after brazing can tell the story (as shown in Figure 3.1).

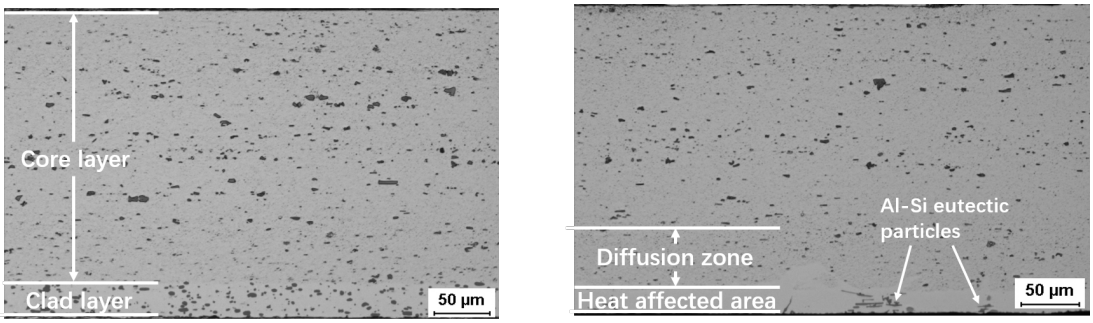

Figure 3.1: Optical images of cross-sections of Alloy FAB913: (a) before brazing; (b) after brazing.

The optical images of cross-section show a strong contrast of the clad layer before and after brazing. During the brazing process, a liquid film forms at the interface between the clad and core layer, and progresses into the core layer. The element distribution changes on the way of liquid film migration [32]. This results in the occurrence of HAZ, which is the zone free of precipitates. The elongated needle-like particles in dark grey are Al-Si eutectic particles. Most of the Al-Si particles accumulated at the surface. They were also detected in between the pre-eutectic

Al grains [33]. In the core layer, different types of intermetallics particles exist with varieties of sizes and chemical composition. Under investigation with EDS, the particles contain Al, Fe, Cu, Mn, and Si elements. These particles are mainly α-Al(Fe,Mn)Si particles. There is also a small amount of AlSiMn and Al6Mn particles existing in the core layer. More details will be discussed in the section below (Section 3.1.3).

After sputtering, craters in different depths were obtained (10 μm, 20 μm, 30 μm, 50 μm and 70 μm). Figure 3.2 shows the topography of sample-FAB913 at the surface and in different depths, respectively. It is obvious that the topography at the surface is completely distinguished compared with those in the craters due to the element distribution.

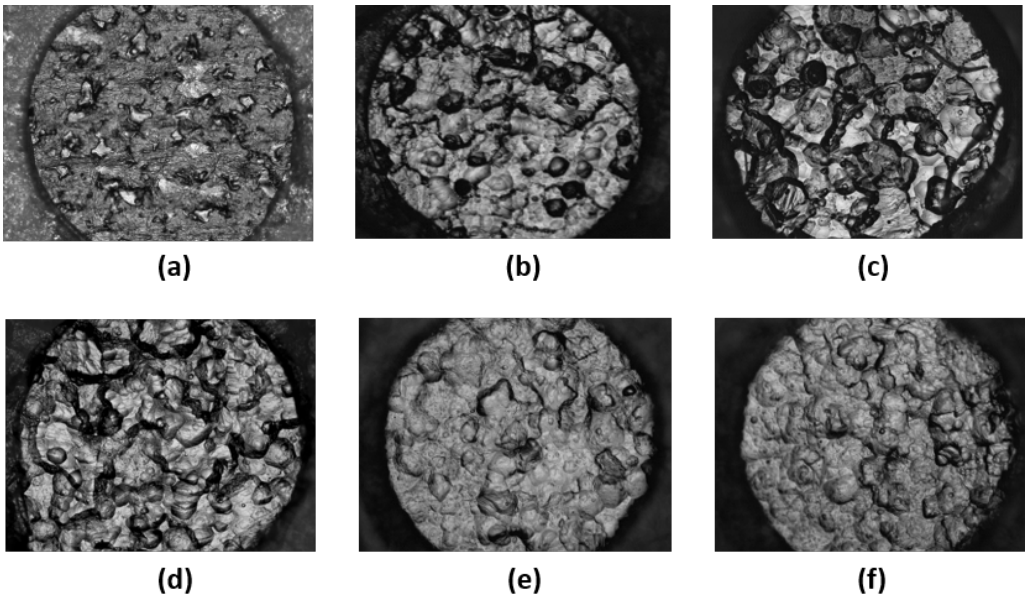

Figure 3.2: The optical images of topography of sample - FAB913 at the surface and in different depths: (a) at surface; (b) 10 μm; (c) 20μm; (d) 30μm; (e) 50μm; (f) 70μm.

The flower-like Al-Si dendrites and α-Al(Fe,Mn)Si particles are the two main features at the surface. Some α-Al(Fe,Mn)Si particles exist near the dendrites. In other depths, the topography did not show evident differences under the optical microscope. More details need to be indicated with the aid of SEM.

The SEM images of the surface in each different depths after GDOES sputtering are shown in Figure 3.3. The size of α-Al(Fe,Mn)Si particles is mostly larger than 1 μm and also can reach up to 20 μm, especially at the clad surface. The α-Al(Fe,Mn)Si particles are commonly smaller in the core layer than in the clad surface, ranging from 1 μm to 10 μm. In the depth of 10 μm, precipitates in slender shape are always Al-Si and a small amount of α-Al(Fe,Mn)Si particles in irregularly round shape with the size of 2-5 μm exist. Another group of particles with size below 1 μm are mainly α-Al(Fe,Mn)Si particles and some are Al_2Cu and Al_6Mn particles. Microstructural characterization is detailed in the next section (Section 3.1.2).

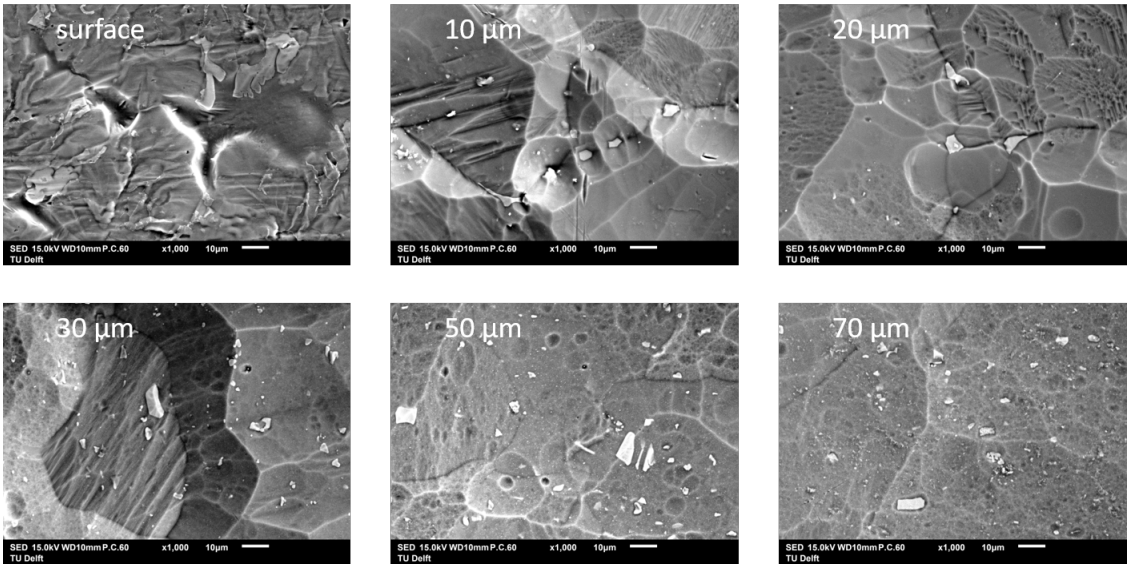

Figure 3.3: SEM images of the surface in each depths of sample - FAB913 after GDOES sputtering.

3.1.2 Elemental Depth Profiling after GDOES sputtering

GDOES depth profiling of system - FAB913 is indicated in Figure 3.4b. To show a more intuitive result, the mass concentration percentages of Mn, Cu, and Fe were multiplied by 50, and Si was multiplied by 2.5. Overall, Si shows a decreasing trend from the surface to the core layer in the brazed material, while other elements had an increasing tendency. In other words, after brazing, Si diffused towards the core layer due to the concentration gradient, which is rich in the clad layer originally. Meanwhile, Mn, Cu, and Fe diffused in the opposite direction - to the clad layer.
There are four distinguished regions existing in the brazed material, marked in Figure 3.4a. The first region is the surface area (0-3μm). Si is the richest alloying element in the 1st region, which comes from the clad material. The second zone is HAZ, which is free of precipitates. According to the GDOES depth profile, in the sample - FAB913, the chemical composition of Si is high in HAZ (approximately 2 - 9.6 wt%), but other alloying elements are relatively low. Cu content is about 0.3 wt%, and the concentration of Fe and Mn is below 0.2 wt%. This could be the reason for the depletion of precipitates in region 2. The third is the diffusion region, which is mainly defined based on the dramatic variation of Mn content. And the fourth region is the core region. The concentration of alloying elements reaches or starts reaching a stable value, which is close to the composition in the core material.

3.1.3 Composition Analysis and Particle Detection

EDS analysis was done at the surface and in the craters to investigate the constituents of the intermetallics particles and the distribution of alloying elements. It was detected that the concentration of Si is high at the surface, especially in the matrix, as shown in both table and EDS map below. There is also the pres-

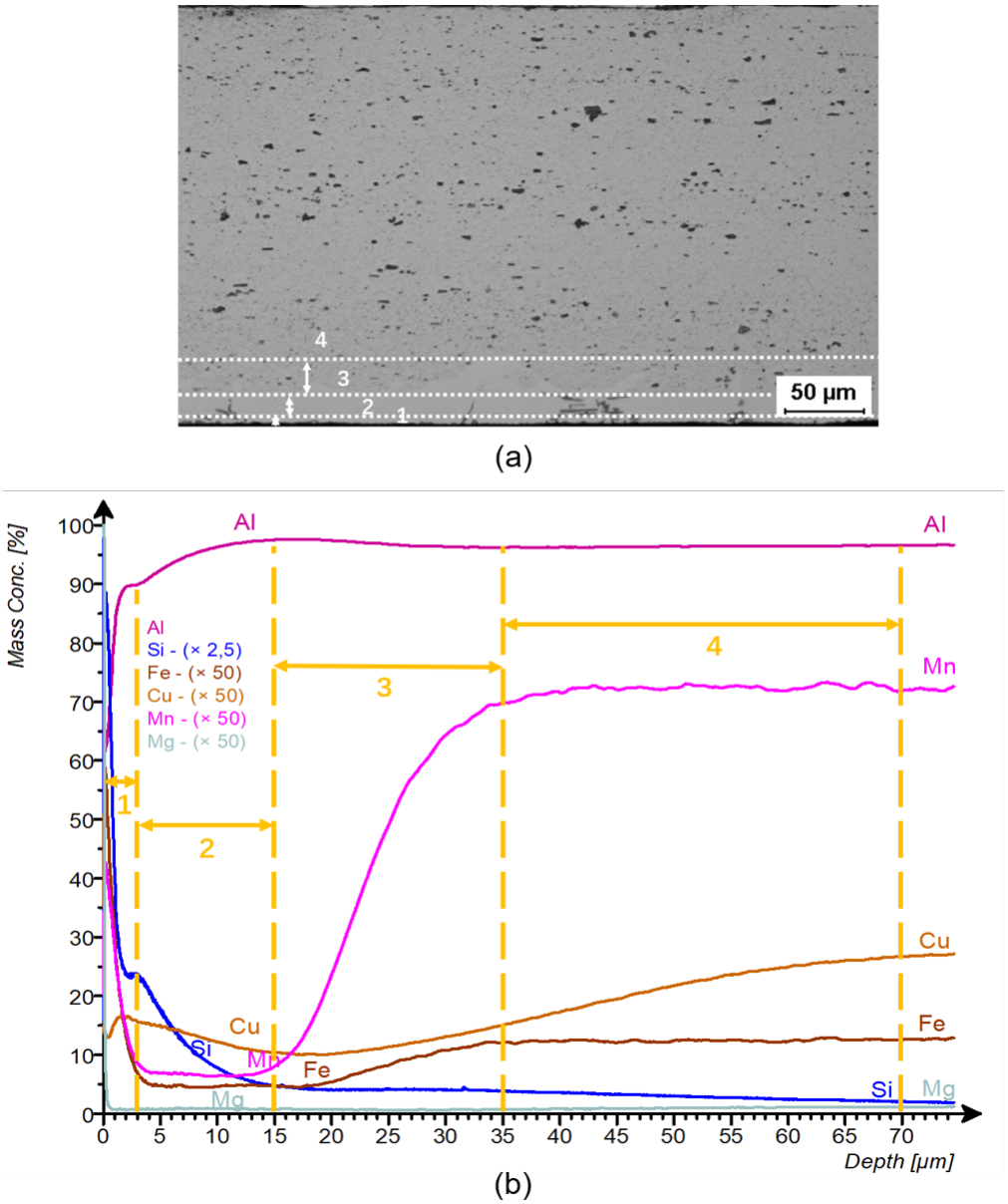

Figure 3.4: (a) GDOES depth profile of Al, Mn, Si, Cu, and Fe of sample - FAB913 and (b) cross-section of sample - FAB913.

ence of some precipitates, including Mn, Fe, and Si elements.

Those flower-like dendrites show Al intersperses among the Si, which is always regarded as Al-Si eutectic phase. The matrix in dark grey is Al matrix. The bright particles with irregular shapes in the matrix are rich in Fe, Si, and Mn.

As mentioned above, there are also some other intermetallics particles in the core layer except for Al-Si and α-Al(Fe,Mn)Si particles. In the sample - FAB913, the other two sub-dominant particles are AlMnSi and Al_6Mn particles. They are shown below in Figure 3.6, and the chemical composition analysis is indicated in Table 3.2. AlMnSi particles were mainly detected in the diffusion layer, while the Al_6Mn particles were mostly found in the core layer. Comparing

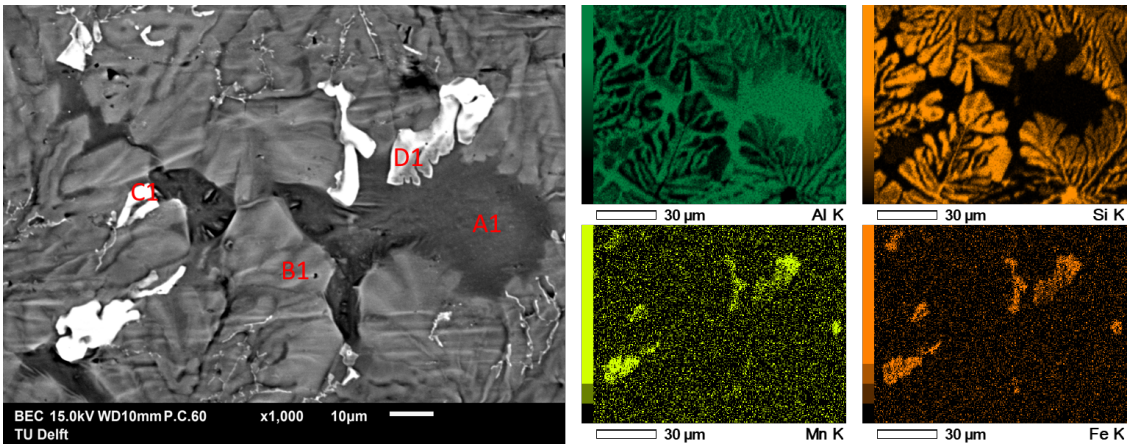

Figure 3.5: SEM back-scattered electron images at the surface of sample - FAB913 and EDS mapping.

Table 3.1: The chemical composition analysis at the surface of sample - FAB913.

Position	Al (wt%)	Si (wt%)	Mn (wt%)	Fe (wt%)
A1	98.38			
B1	41.34	57.25		
C2	89.46	1.94	1.18	5.73
D2	71.37	5.82	5.82	10.08

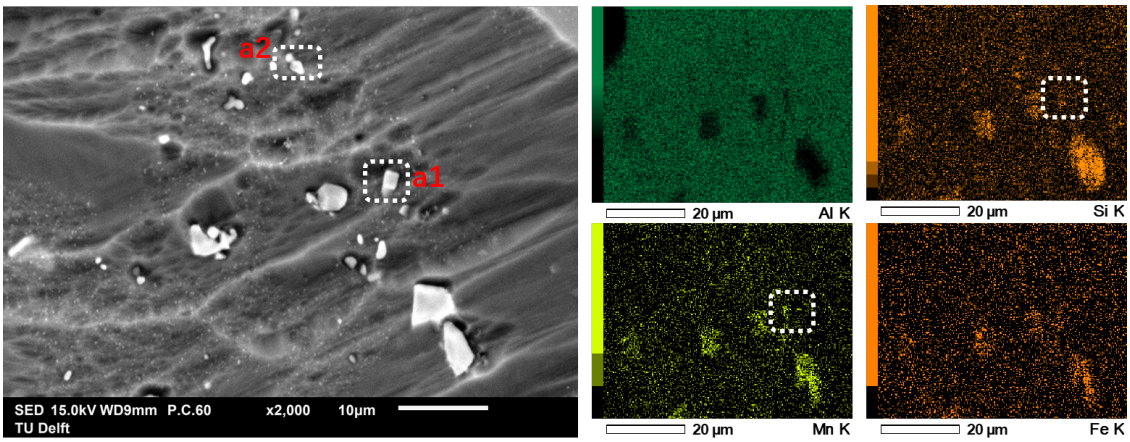

(a)

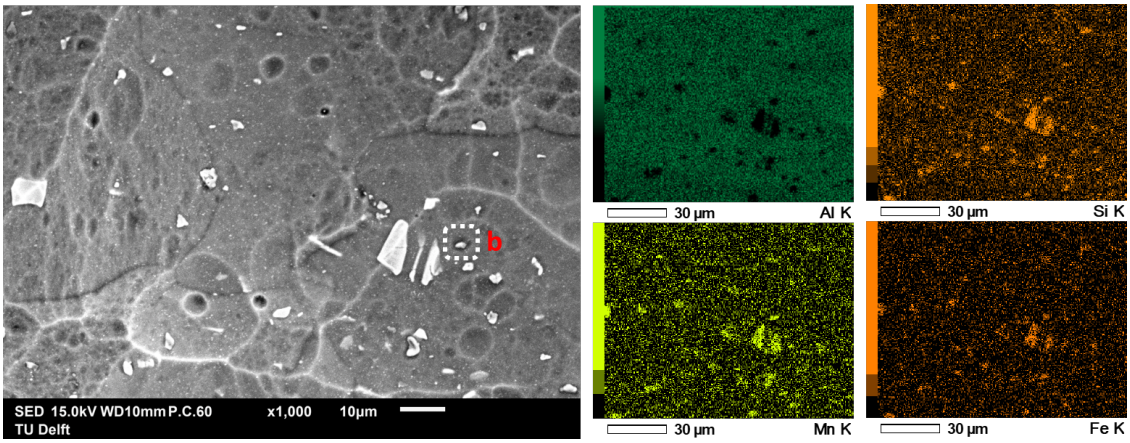

(b)

Figure 3.6: Analysis of other intermetallics particles in FAB913: (a) AlMnSi; (b) Al_6Mn.

Table 3.2: The chemical analysis of other intermetallics particles in FAB913.

Position	Al (wt%)	Si (wt%)	Mn (wt%)
a1	66.44	0.69	1.18
b	60.17		0.80

to α-Al(Fe,Mn)Si particles, the amount of these intermetallics particles is small. AlMnSi particles are always in an irregular shape, while Al_6Mn was found in the core layer of the sample - FAB913 with a round shape.

3.1.4 Electrochemical Analysis

OCP Results

The samples were immersed in a 0.05 M NaCl solution with 0.5 ml/L H_2O_2 for 15 minutes prior to the polarization experiment to check if they reached a thermodynamically equilibrium state. The OCP curves are shown in Figure A.1 (One of the repetition is presented here). Almost all of the OCP values achieved a stable level after 6 minutes. The overall trend of the curves is stable due to the addition of H_2O_2. Its high oxidizing ability makes samples quickly oxidized and leads to the formation of a protective oxidation layer. Except for the OCP values measured at the surface of the samples, they scattered (shown in black), revealing the high activity in this region.

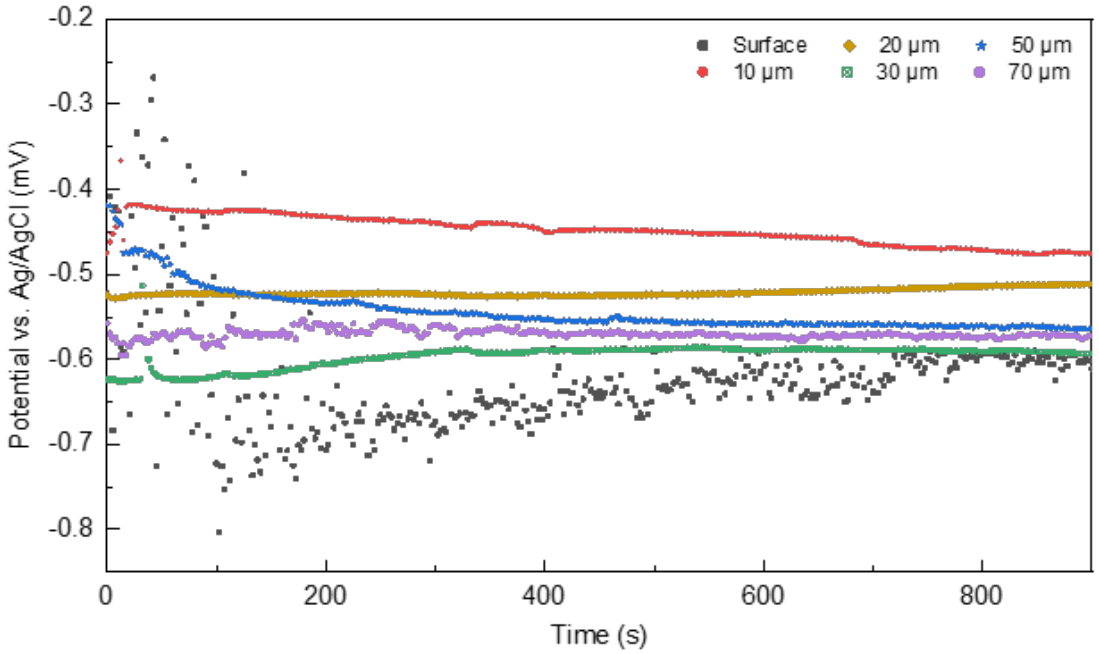

Figure 3.7: OCP curves of sample - FAB913 at different depths in 0.05 M NaCl solution with 0.5 ml/L H_2O_2.

The average OCP at the surface is the least noble one. In the depth of 10 and 20 μm, the OCP values are significantly higher than in the other depths and approximately 100 mV higher than at the surface. The order of the average OCP

values from low to high is : surface $<$ 30 μm $<$ 70 μm $\approx$ 50μm $<$ 20 μm $<$ 10 μm.

Anodic and Cathodic Polarization

The polarization curves are shown in Figure A.3 (curves for 2 repetitions are shown in Appendix). Focusing on the anodic part of the polarization curve, active oxidation reactions took place. The surface of the clad layer is extremely active according to the rapidly increasing current densities when apply a small value of potential to the working electrode. The current density increased a hundred times and the potential has only increased 10 mV. The corrosion current density at the surface is around 0.5 mA/cm^2. As for the other part of the polarization curve, the cathodic curves obtained at the surface show a phenomenon of diffusion limitation. The dissolved oxygen was not enough for the reduction reaction, so that the current density was limited. Overall, the corrosion potentials and current densities of the inner layers are nobler and smaller than at the surface.

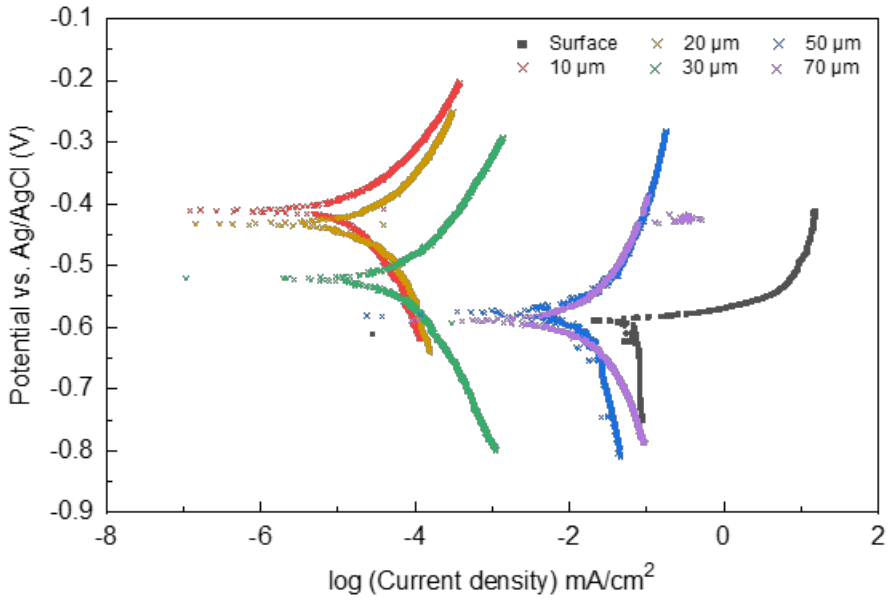

Figure 3.8: Polarization curves of sample - FAB913 at different depths in 0.05 M NaCl solution with 0.5 ml/L H2O2.

The corrosion current densities tested in the depth of 10 and 20 μm are almost three to four orders of magnitude smaller than at the surface. And the corrosion potentials in these two depths are the highest. In the depth of 50 and 70 μm, although the corrosion potential is closer to the corrosion potential at the surface, the values of current density are approximately dozens of times smaller. The result is scattered in the depth of 30 μm, the reason could be the non-homogeneous distribution of particles.

3.1.5 Corrosion Morphology

After the electrochemical measurements, the microstructure has definitely changed, OM and SEM were applied to investigate the evolution of microstructure after polarization.

The change at the surface by corrosion is macroscopic. The area after polarization turned to dark-grey according to Figure 3.9a. Comparing the image obtained under optical microscopy before (Figure 3.2a) and after (Figure 3.9b) polarization, it is obvious that the Al-matrix was preferentially corroded while the dendrites did not show distinct change.

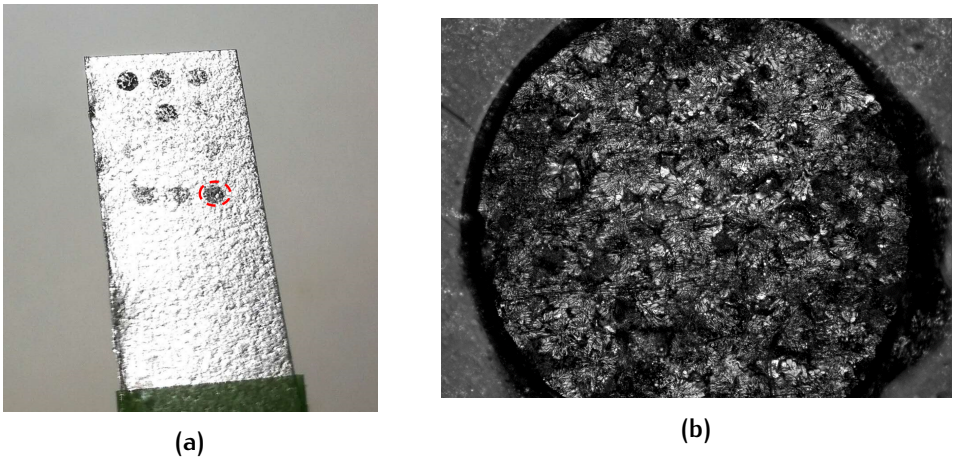

(a) (b)

Figure 3.9: Images of surface of FAB913 after polarization: (a) by naked eye; (b) by OM.

The SEM image shows more details (Figure 3.10). Corresponding to the elemental distribution maps, oxides formed on the Al-matrix during corrosion and α-Al(Fe,Mn)Si particles remained. The dendrites look more obtrusive, the color near the dendrites became darker and "ditches" appeared among the dendrites due to the dissolution of Al. There are also Cl elements detected in the matrix because of the use of NaCl solution.

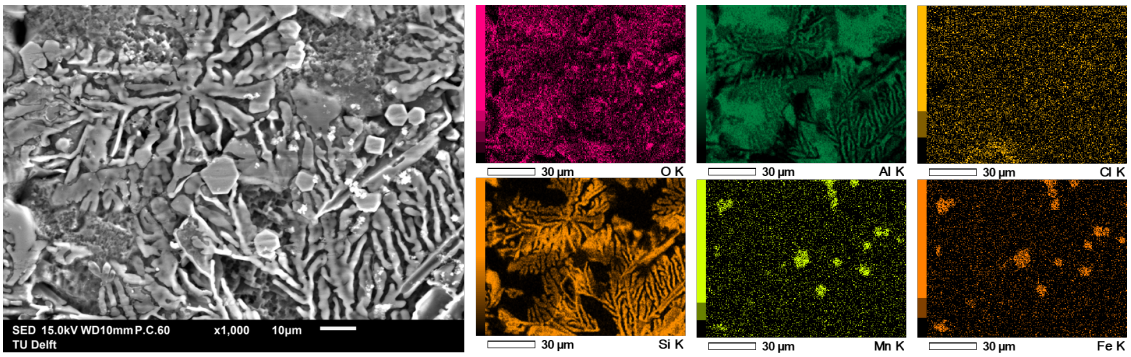

Figure 3.10: SEM image at the surface of sample - FAB913 after polarization.

However, sometimes, tiny changes in microstructure such as the formation of small pits are invisible through the naked eyes or optical microscopy, which can be observed via SEM.

According to Figure 3.11, some features evidently indicate the microstructural evolution after polarization. The most significant is the generation of two small pits, as shown in the red dotted circle, although the applied potential to the working electrode did not reach to a pitting potential. This is the evidence of de-alloy phenomenon of particles. Additionally, the grain boundaries through the matrix look more obvious. It is also noticed that trenches appeared surrounding the particles. (for example, the rectangular-like particles at the left-side of the image.)

Figure 3.11: SEM images at the depth of 50 μm of sample - FAB913 before (left) and after (right) polarization.

3.1.6 SKPFM

The Volta potential difference and topographical maps were scanned with a size of 50 μm x 50 μm at the cross-section from the surface of the re-solidified clad layer to the core layer. The acquired maps were arranged on the same level to show the situation at the whole cross-section intuitively. The result of the maps and line scan section analysis through the cross-section of FAB913 are presented in Figure 3.13 and Figure 3.12.

In the topography maps, the interface between the re-solidified clad layer and resin is obvious shown at the left-side of Figure 3.13(a). Other information that can be obtained from topography maps is polish-remained scratches and the existence of intermetallic particles. However, not all the particles can be seen in the topography maps, but they can be clearly identified in the Volta potential amps. For example, in Figure 3.13(g), there are plate-like intermetallic particles embedded in the matrix, while in Figure 3.13(b) the feature is not evident. The Volta potential of that particle is approximately 50 mV higher than the surrounding matrix. The positive value indicates that this particle would behave as a cathode when the matrix gets corroded.

Three line scan analysis was conducted at three different horizontal levels in the cross-section region, as shown in the Volta potential maps in Figure 3.13 and the

corresponding Volta potential curves are sketched as a function of depth (which is the distance from the surface to the core layer). According to the figure, the overall potential variation trend of three curves are similar. At the surface of clad layer, the Volta potential is very low, illustrating the anodic nature in this area. In the region between 10 and 20 μm, the Volta potential shows a positive value, which corresponds to the HAZ and diffusion zone. These two regions were tested to be the noble area in the electrochemical experiments compared to the surface. In the more deeply region (core layer), the value fluctuates around the "zero" line.

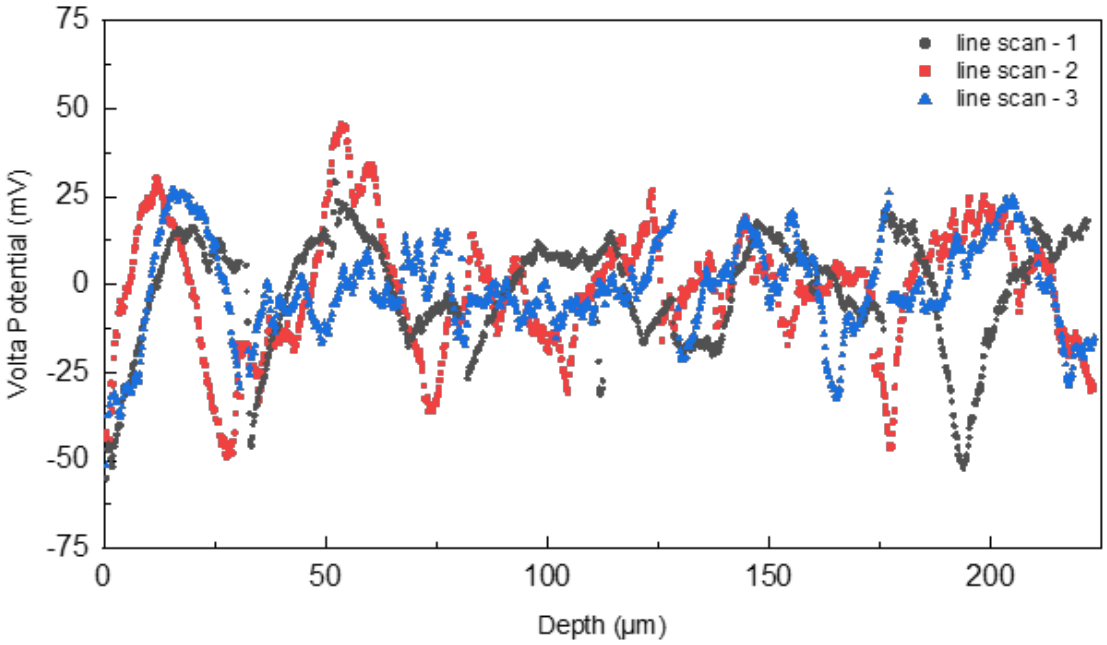

Figure 3.12: Volta potential variation through the cross-section of FAB913.

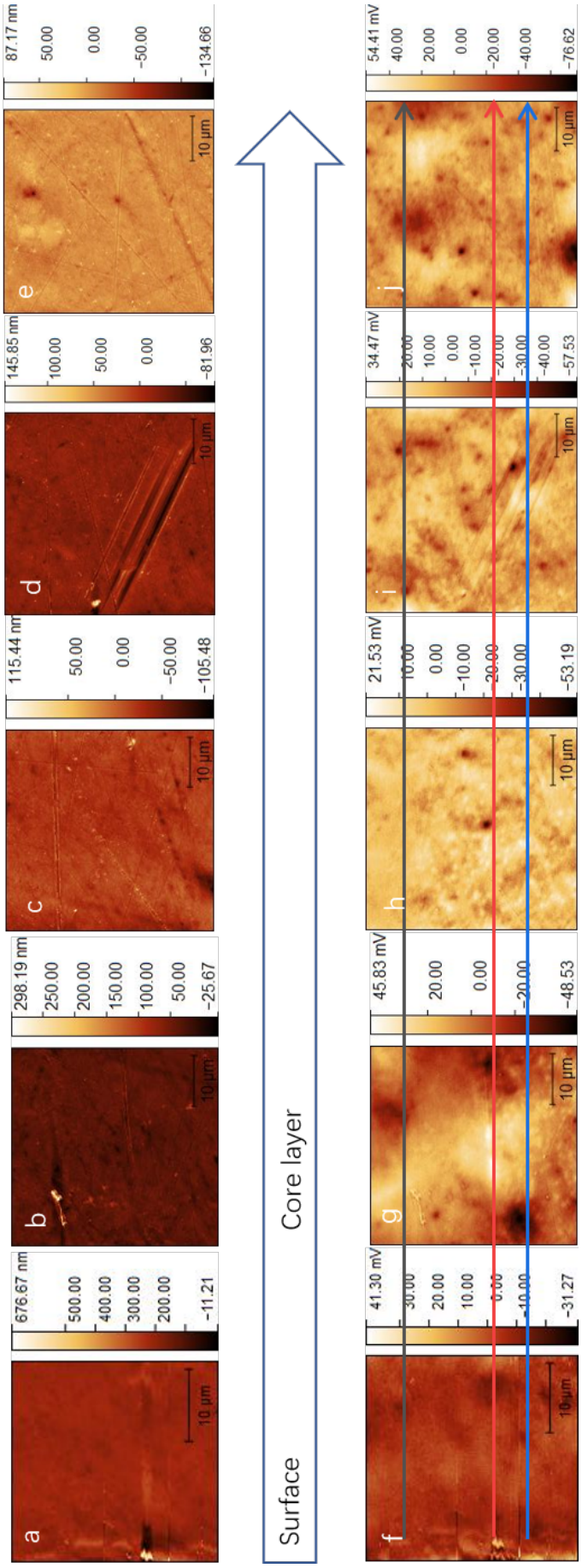

Figure 3.13: SKPFM result of alloy FAB913: (a) to (e) are topography maps, (f) to (j) are Volta potential maps.

3.2 SYSTEM 8125

3.2.1 Microstructural Analysis

Optical images of the cross-section of the material 8125 before and after brazing are shown in Figure 3.14. It is the same as the sample - FAB913 that at the surface of the clad layer, the elongated coarse particles in dark grey are Si particles. A wider variety of intermetallic particles exists in the core layer. In the diffusion zone, two types of particles are distinct, based on the difference of sizes. One is the particles that are smaller than 1 μm. And the other group contains the particles with a larger size that can reach up to 20 μm. The dominant particles in the core layer are α-Al(Fe,Mn)Si particles with both sizes. Other species of particles also exist in the 8125 core layer with a wider variety than in the FAB913. More details will be discussed in the next section (Section 3.2.2).

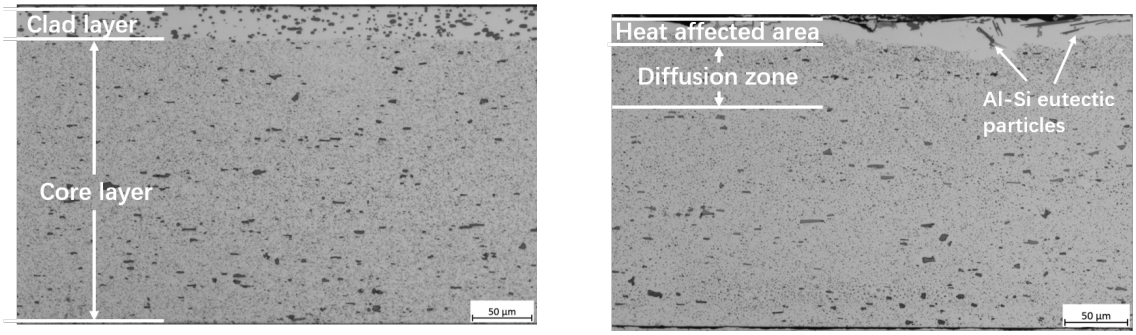

Figure 3.14: Optical images of cross-sections of Alloy 8125: (a) before brazing; (b) after brazing.

Figure 3.15 shows the appearance of the surfaces in different depths of alloy 8125, respectively. Same as the sample - FAB913, the topography at the surface shows a completely different picture with the comparison of topography in the inner layer due to the accumulation of the Al-Si eutectic phase. And the topography at the surface in both systems is resembled due to their similar composition. Distinct grain boundaries were shown in the image of depth of 10 μm. More details of the microstructure in each depth can be shown in the SEM images (Figure 3.16).

Focusing on the SEM image gained at the surface, the flower-like dendrites and the Al-matrix in darker grey are the two distinct features. The particles with irregular shapes distributed among the dendrites are α-Al(Fe,Mn)Si particles. It is worth to mention that the small holes in the Al-matrix are solidification shrinkage voids normally formed during the brazing process. During solidification of the clad layer, the primary α-Al grains form firstly and Al-Si eutectic phase accumulates at the surface, contributing to the formation of shrinkage voids [33]. In the depth of 10 μm, it shows a evident difference compared to the inner layer. Lathy particles in light grey are embedded in the grain boundaries. These are Al-Si particles. And because it is located in the HAZ, the amount of intermetallics is relatively lower than in the other depths, which is also proved by the SEM

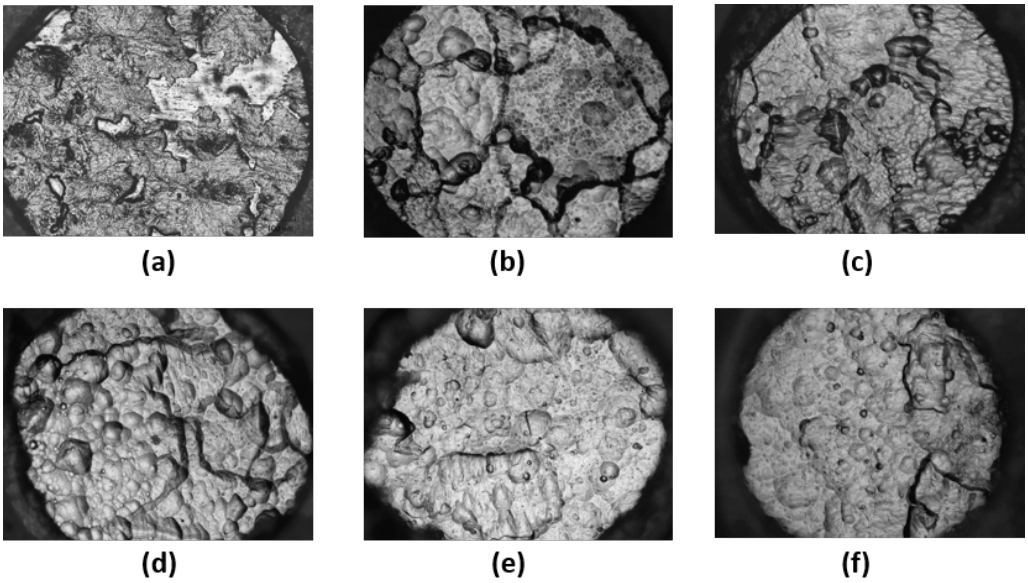

Figure 3.15: The optical images of topography of sample - 8125 at the surface and in different depths: (a) at surface; (b) 10 μm; (c) 20μm; (d) 30μm; (e) 50μm; (f) 70μm.

image. As for in the rest of the depths, SEM images show similar features - intermetallics distribute in the Al-matrix. Some of the intermetallic particles gather in the Al-matrix as a group, some of them distribute separately. Most of the particles are α-Al(Fe,Mn)Si particles. A small number of other species of particles also exist with the consituents of Cu, Mn, Fe, and Si. Microstructural characterization is detailed in the next section (Section 3.2.2).

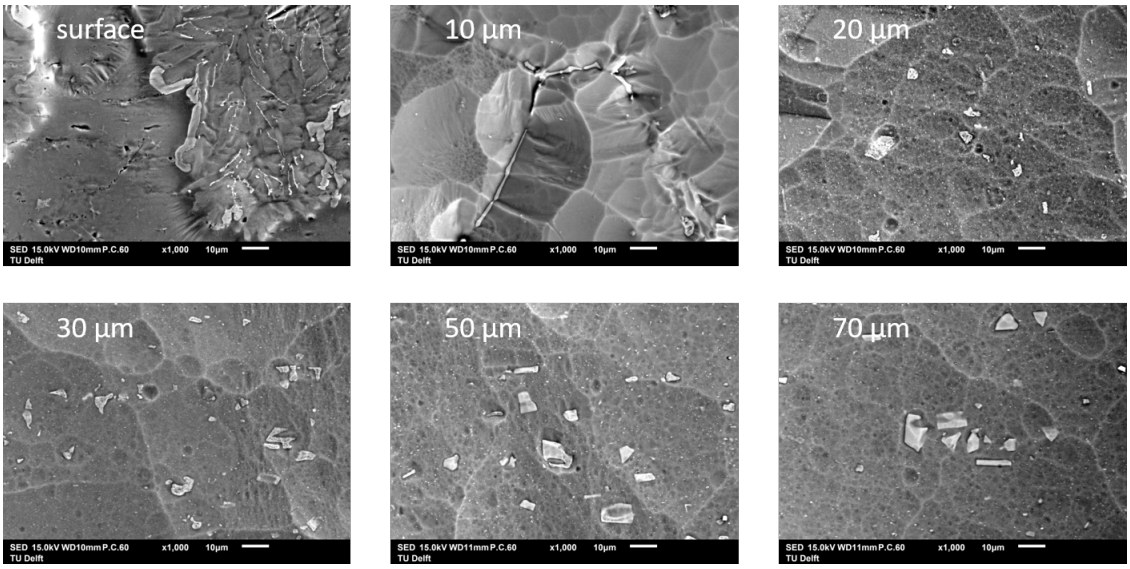

Figure 3.16: SEM images of the surface in each depths of sample - 8125 after GDOES sputtering.

3.2.2 Elemental Depth Profiling after GDOES sputtering

GDOES depth profiling of sample - 8125 is shown in Figure 3.17b. Corresponding to the optical image (Figure 3.17)a, the cross-section of brazed aluminium sheet 8125 also can be divided into four distinguished regions.

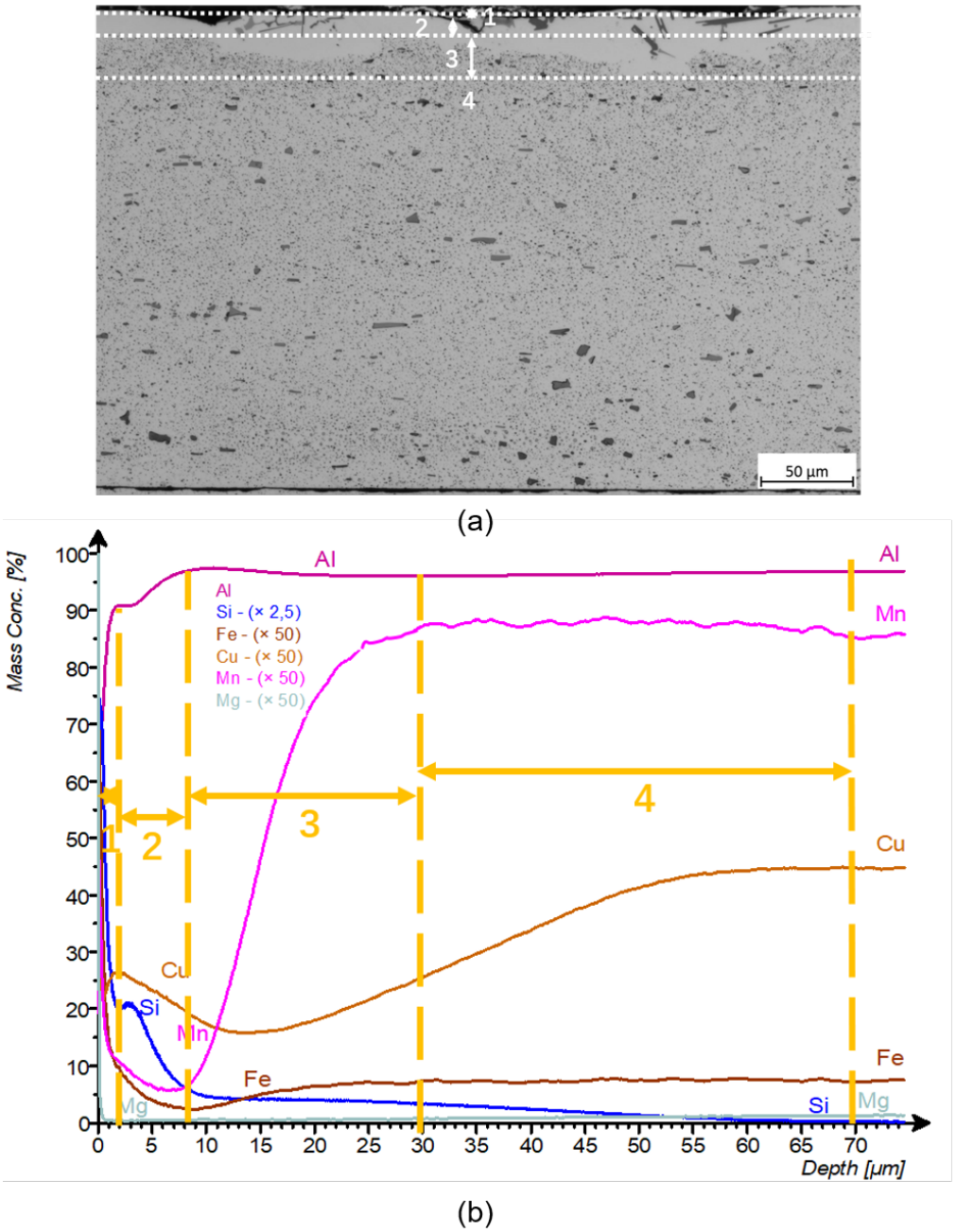

Figure 3.17: (a) cross-section of sample - 8125 and (b) GDOES depth profile of Al, Mn, Si, Cu, and Fe of sample - 8125.

The first region is the surface area, from 0 to 2 μm. Undisputedly, Si is the richest alloying element at the surface due to the accumulation of the Al-Si phase. The second zone is heat affected zone. The HAZ in the brazed 8125 is thinner than that in the brazed FAB913, ends at around 9 μm. In this region, Si content is

still high (approximately 2.4 - 8 wt%), Cu content is between 0.38 and 0.52 wt%, and the concentration of Fe and Mn is below 0.2 wt%. The diffusion zone is the third region, ranging from 9 to 30 μm. Looking through the whole trends of the elemental variation, the change of element concentration of Mn and Cu is greater than in FAB913, while the change of Fe is relatively smaller. This is because the concentration of Mn and Cu is higher in the core layer and Fe content is lower in this system. The greater concentration gradient leads to a more dramatic diffusion. Cu and Fe from the core layer diffused to the clad layer and Si from the clad layer diffused towards to opposite direction. In the diffusion zone, Mn content shows a wide range, between 0.12 and 1.7 wt%. The fourth region is the core layer. Mn and Fe almost reach a stable level at the start of this region, while Cu and Si contents are still changing.

3.2.3 Composition Analysis and Particle Detection

As mentioned above, the Al-matrix with solidification shrinkage voids, Al-Si eutectic phase and particles with constituents of Fe, Mn, Si are the main features at the surface. It is worth noticing that some of the particles in the sample - 8125 also contain Cu element. The elemental distribution maps correspond to the localized chemical composition analysis, but some elemental maps are missing due to the limited elemental content and device performance.

According to the BSE image shown in Figure 3.18, it shows that at the surface, the size of α-Al(Fe,Mn)Si particles containing with Cu can even reach up to 30 μm, which is larger than those in the inner layer. The α-Al(Fe,Mn)Si particles exist at the surface have two main shapes: irregular shape and filamentous shape.

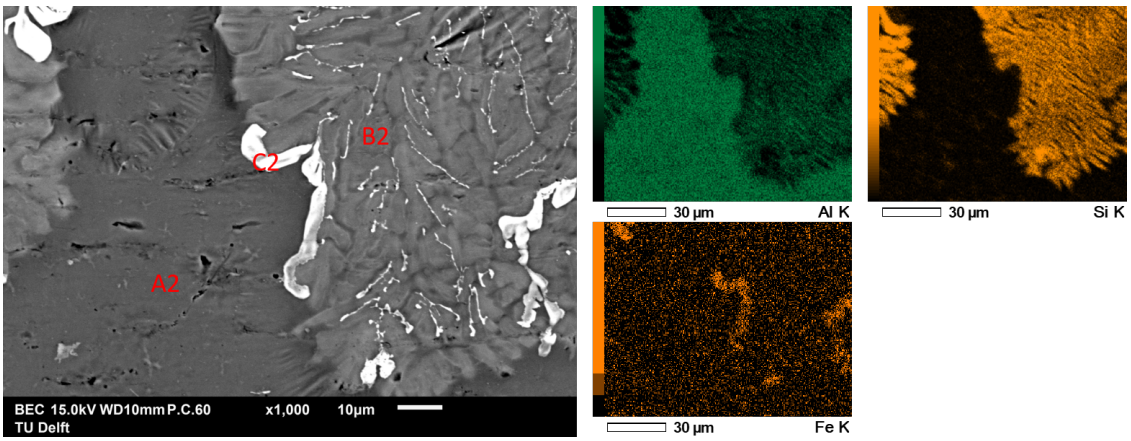

Figure 3.18: SEM back-scattered electron images at the surface of sample - 8125 and EDS mapping.

The types of intermetallic particles in the inner layer are more diverse. As indicated in Figure 3.19 and Table 3.4, there are four species of particles existing in the inner layer except for Al-Si and α-Al(Fe,Mn)Si particles. Both amount and size of these particles are smaller if compare to α-Al(Fe,Mn)Si particles. AlMnSi and AlMnFe particles were found in the diffusion zone and core layer with irregular shape and size between 5 and 10 μm. Al_2Cu and Al_6Mn were mostly

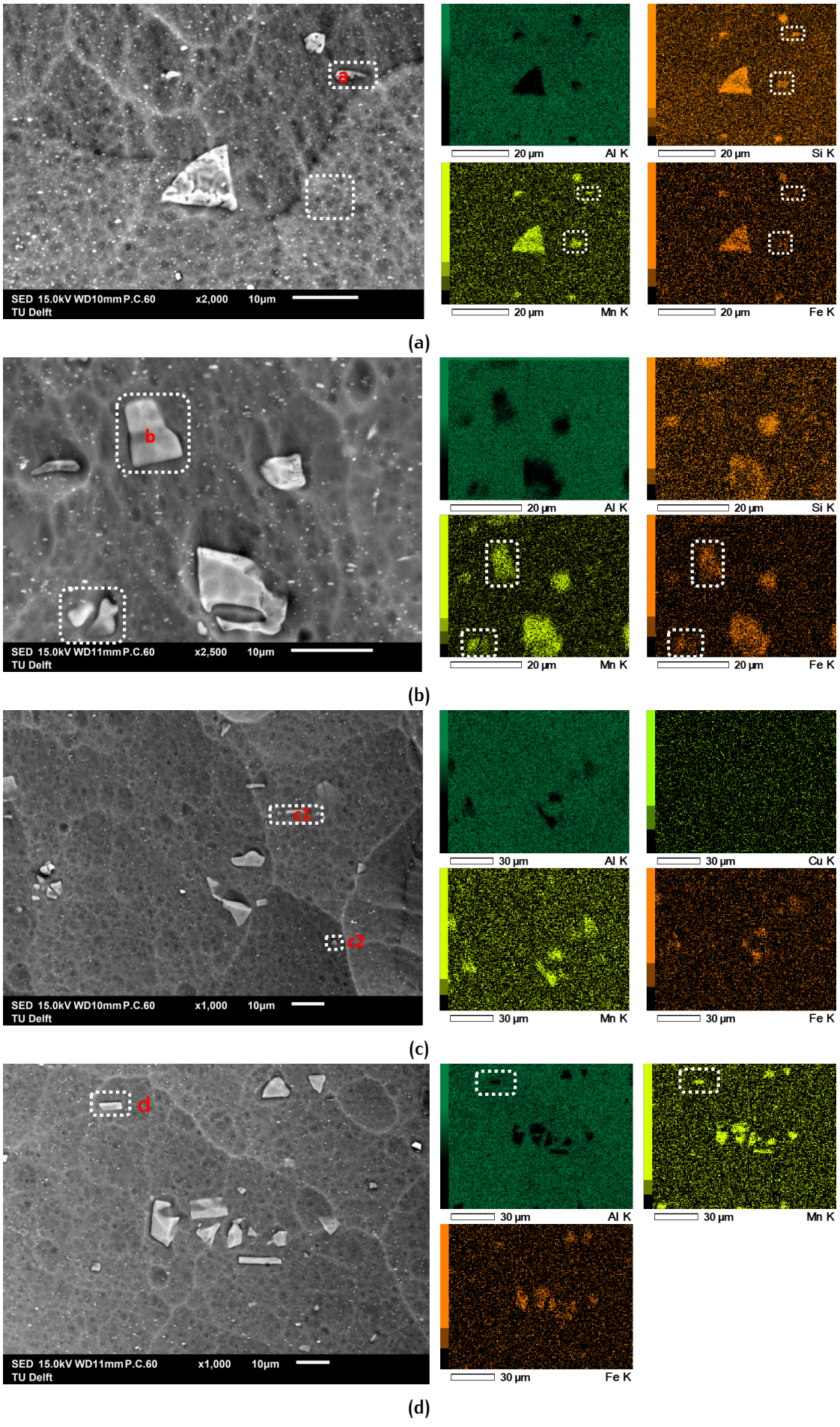

Figure 3.19: Analysis of other intermetallics particles in Alloy 8125: (a) AlMnSi; (b) AlMnFe; (c) Al_2Cu; (d) Al_6Mn.

Table 3.3: The chemical composition analysis at the surface of sample - 8125.

Position	Al (wt%)	Si (wt%)	Mn (wt%)	Fe (wt%)	Cu (wt%)
A2	100				
B2	74.56	23.99			
C2	64.10	4.76	11.13	16.64	2.28

detected in the core layer with a round or plate-like shape. The size of them can reach up to 8 μm, but some Al_2Cu particles also exist with the size below 1 μm.

Table 3.4: The chemical analysis of other intermetallics particles in sample - 8125.

Position	Al (wt%)	Si (wt%)	Mn (wt%)	Fe (wt%)	Cu (wt%)
a	67.80	0.62	4.68		
b	52.89		8.61	3.80	
c1	86.52				1.01
c2	98.41				1.59
d	60.17		0.80		

3.2.4 Electrochemical Analysis

OCP Results

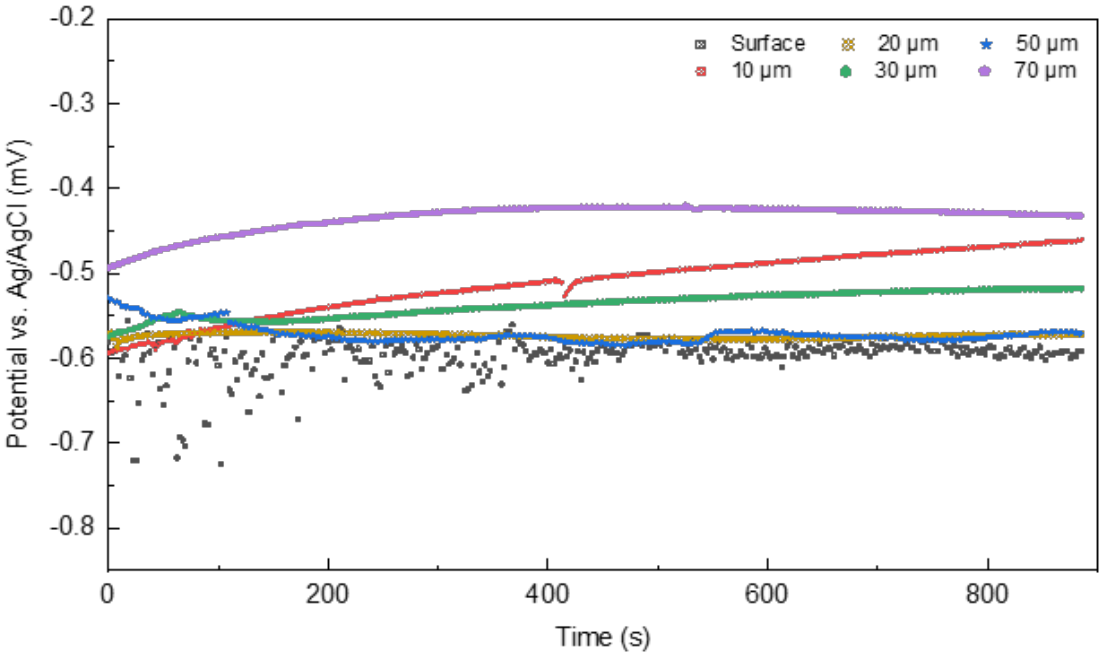

Figure 3.20: OCP curves of sample - 8125 at different depths in 0.05 M NaCl solution with 0.5 ml/L H_2O_2.

In the case of sample - 8125 which has been immersed in 0.05 M NaCl solution with 0.5 ml/L H_2O_2 for 15 minutes before the polarization experiment, it took

approximately 10 minutes on average reaching to a thermodynamically equilibrium state. The OCP curves are shown in Figure A.2. The trend of some OCP vs. time curves increased, indicating that it was resistant to the aggressive environment and forming a protective oxidation film during the exposure. Like the other system - FAB913, the OCP values measured at the surface were scattered (shown in black), illustrating the high reaction activity at the re-solidification surface. The surface was dominantly affected by localized corrosion.

The average OCP at the surface is the least noble one and in this scenario of sample -8125, the OCP values in the depth of 20 and 50 μm are very close to the values at the surface. In the depth of 70 μm, the OCP values are much higher than in the other depths. The order of the average OCP values from low to high is : surface $<$ 20 μm $\approx$ 20μm $<$ 30 μm $<$ 10 μm $<$ 70 μm.

Anodic and Cathodic Polarization

The current densities were recorded with a sweep speed of 0.5 mV per second, the polarization curves present the potential as a function of current density, as shown in Figure A.4 ((curves for 2 repetitions are shown in Appendix)). Corresponding with the previous investigation results, the anodic part of the polarization curve obtained at the surface indicates the dramatic increase of current density, revealing the high reaction activity and localized corrosion attack also took place in sample - 8125. The variation of current density can be count as two orders of magnitude when the potential only increased by several millivolts. The corrosion current density at the surface of the sample- 8125 is approximately 0.8 mA/cm^2. The cathodic part of the curves obtained at the surface also shows a diffusion limitation phenomenon due to lack of the dissolved oxygen. Overall, the corrosion potentials and current densities in the inner layers show better corrosion response than at the surface.
In the case of sample-8125, the average corrosion current densities in the depth of 50 μm are 10 times smaller than at the surface, while the other depths are hundreds of times smaller. The corrosion potential obtained at 50 μm is close to that at the surface, only 5 mV higher. The corrosion response in the depth of 50 μm is more active than in the other depths. In the depth of 70 μm, the corrosion potential is the highest and corrosion current density is very low, approximately 3x10^{-5} mA/cm^2.

3.2.5 Corrosion Morphology

The change of the surface at each depths after polarization in the electrolyte was investigated. Corresponding to the electrochemical response, localized corrosion attack should happen at the surface, the same result was gained from the pictures took under the optical microscope (Figure 3.22).

A strong contrast show on the surface before and after the polarization experiment. It is obvious that the Al-matrix got severe corroded and the color of the

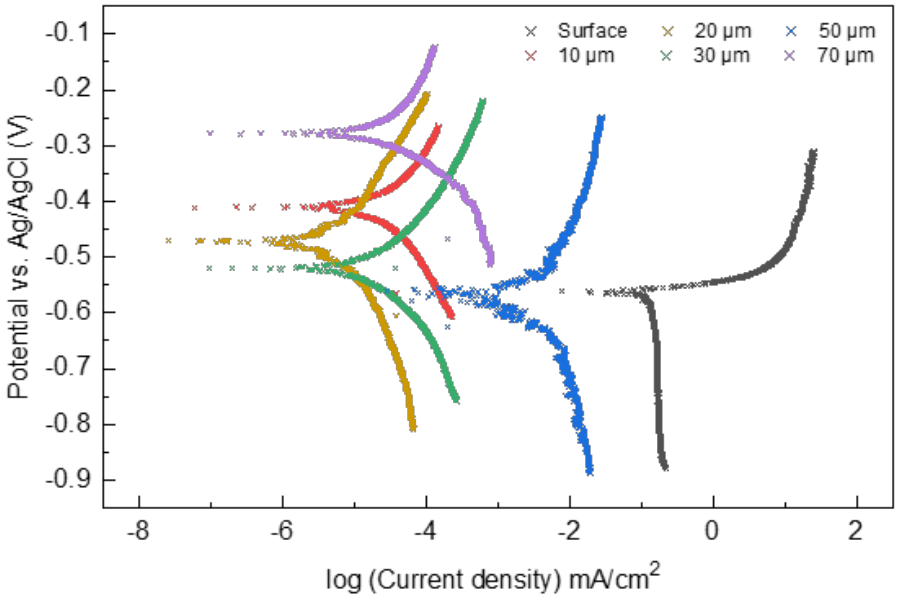

Figure 3.21: Polarization curves of sample - 8125 at different depths in 0.05 M NaCl solution with 0.5 ml/L H_2O_2.

matrix switch from light-grey to dark-grey. The dendrites were not the relatively preferential corrosion sites. More details can be revealed according to SEM images with high magnification.

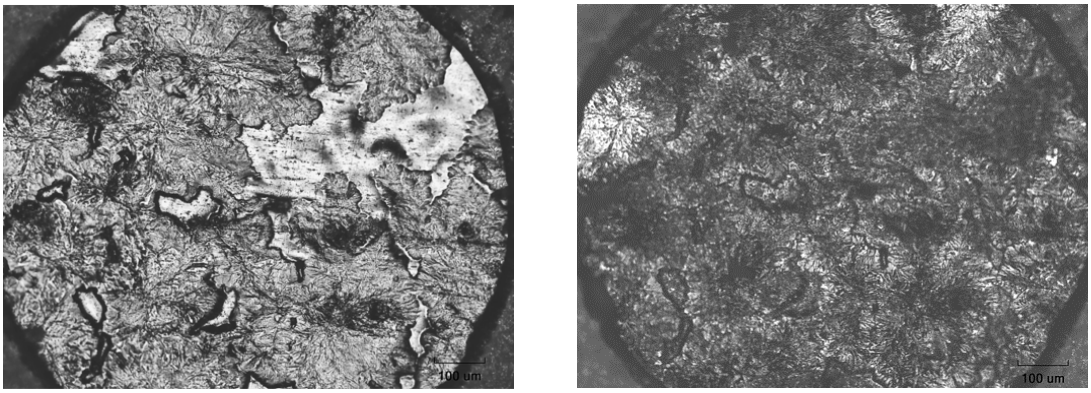

(a) (b)

Figure 3.22: Optical image of the surface of alloy - 8125 before (a) and after (b) polarization.

The SEM image further proved the severity of corrosion attack at the surface (Figure 3.23). Combing with the elemental distribution maps obtained from EDS analysis, it shows that the Al-matrix was terribly corroded and became porous. Corrosion of the matrix also attributes to the formation of oxides as shown in the distribution map of O - O mainly distributes at the corrosion sites. The dendrites protruded from the matrix, and they look "more clearly" after polarization because the Al interspersed in the dendrites was dissolved. The elemental map of other elements illustrates that the polarization experiment hardly influenced the Si dendrites and intermetallic particles consisting of Mn, Fe, and Si.
In the inner layer of sample - 8125, the change of morphology was not equally

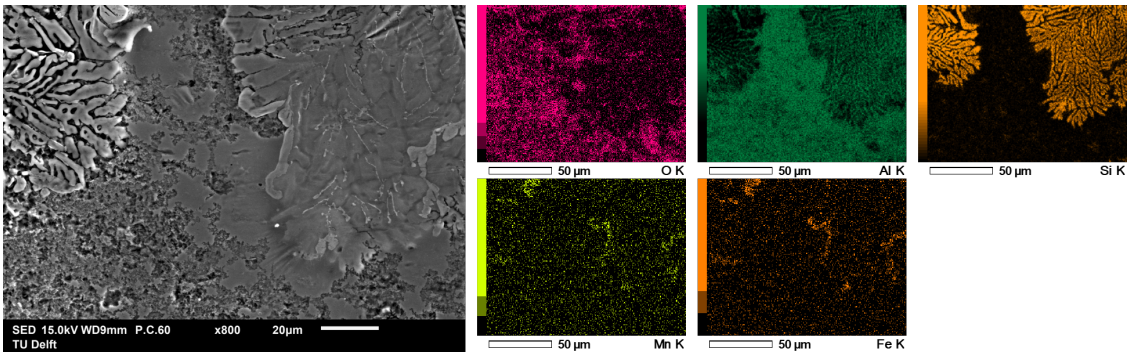

Figure 3.23: SEM image at the surface of sample - 8125 after polarization.

obvious as at the surface, however some features still can be regarded as the evidence of microstructural evolution during the exposure to the electrolyte. As shown in Figure 3.24a, in the red dotted circle at the top-side of the image, the intermetallic particle was surrounded by a continuous trench. The reason for the occurrence of the trench could be assumed that the attack was already existed before polarization. Looking through the image shot after polarization, it seems like the particle was moved out of the matrix. There was a hole remained in the matrix, which is the evidence of the fact that the particle dealloyed. Furthermore, the grain boundary located through the matrix looks more distinct.

Comparing with Figure 3.24a, Figure 3.24b is more like a step in the dealloy procedure. There are two distinct grooves existing at the two sides of the particle AlMnSi and at the interface between the particle and the matrix. The trenches became wider around the particle after polarization. And it can be assumed that the trenches penetrated into the matrix, which is regarded as the former step of the end of dealloy.

3.2.6 SKPFM

Each of the Volta potential difference and topographical maps were scanned from the interface between resin and sample to the core layer with a size of 50 μm x 50 μm. The valid cross-section maps gained for alloy 8125 are approximately 175 μm long, as shown in Figure 3.25.

In the Volta potential maps, the easiest feature that can be discovered is always the intermetallic particles. Focusing on Figure 3.25(h), a round-shape spot exists in the middle of the map, commonly considered as the cathodic-behave intermetallic particle.

In the topography maps of sample 8125, there is a "hole" existing in the matrix in Figure 3.25(b), which could be a small pit. With the combination of the Volta potential map Figure 3.25(f), the pit shows negative value while the surrounding areas show positive value. The Volta potential difference at this pit site could be a driving force to accelerate the corrosion attack.

Meanwhile, the scratches in the matrix are also proved as the preferentially cor-

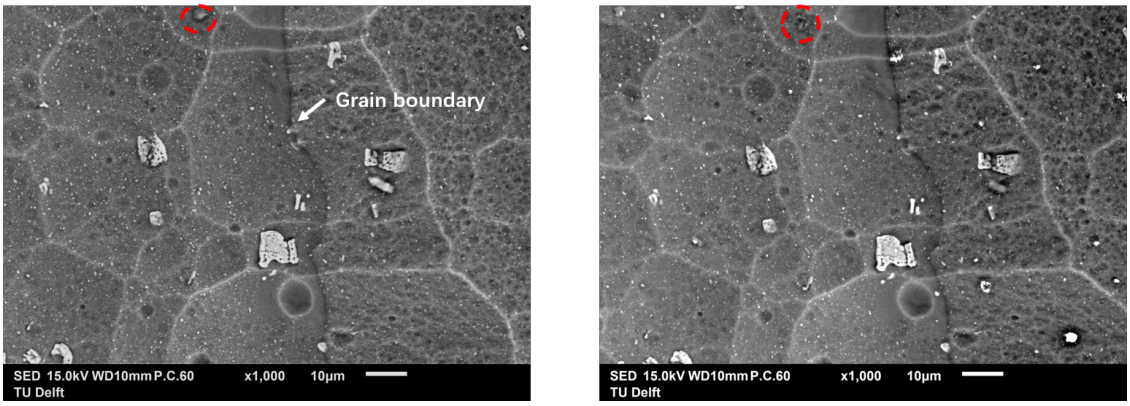

(a) SEM image with magnification 1000x before (left) and after (right) polarization.

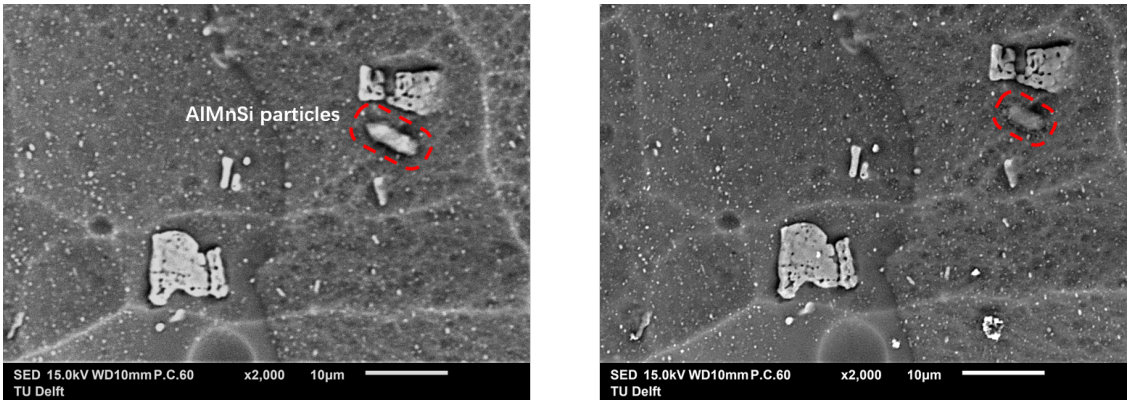

(b) SEM image with magnification 2000x before (left) and after (right) polarization.

Figure 3.24: SEM images showing microstructural evolution at the depth of 30 μm of sample - 8125.

roded sites. It can be noted that some scratches are still left on the surface after polishing. According to Figure 3.25(d) and Figure 3.25(h), the Volta potential in the scratch is low and the value at the edge is high, explaining the reason why the damaged spots in the material are much easier to be corroded.

Three separate line scan analyses through the cross-section of alloy 8125 are presented in three different color, the Volta potential curves are shown in Figure 3.26. Comparing with the core layer, the surface of the re-solidified layer has high reaction activity. That is the reason why the surface show such a low Volta potential. Then, the value almost fluctuates in a range of + 30 mV to - 30 mV in the inner layer, neglecting the peaks due to intermetallic particles. The distinct peak at the end of line scan - 1 corresponds to the round-shape intermetallic particle in the Volta potential map (h). The Volta potential difference between that particle and matrix is around 100 mV.

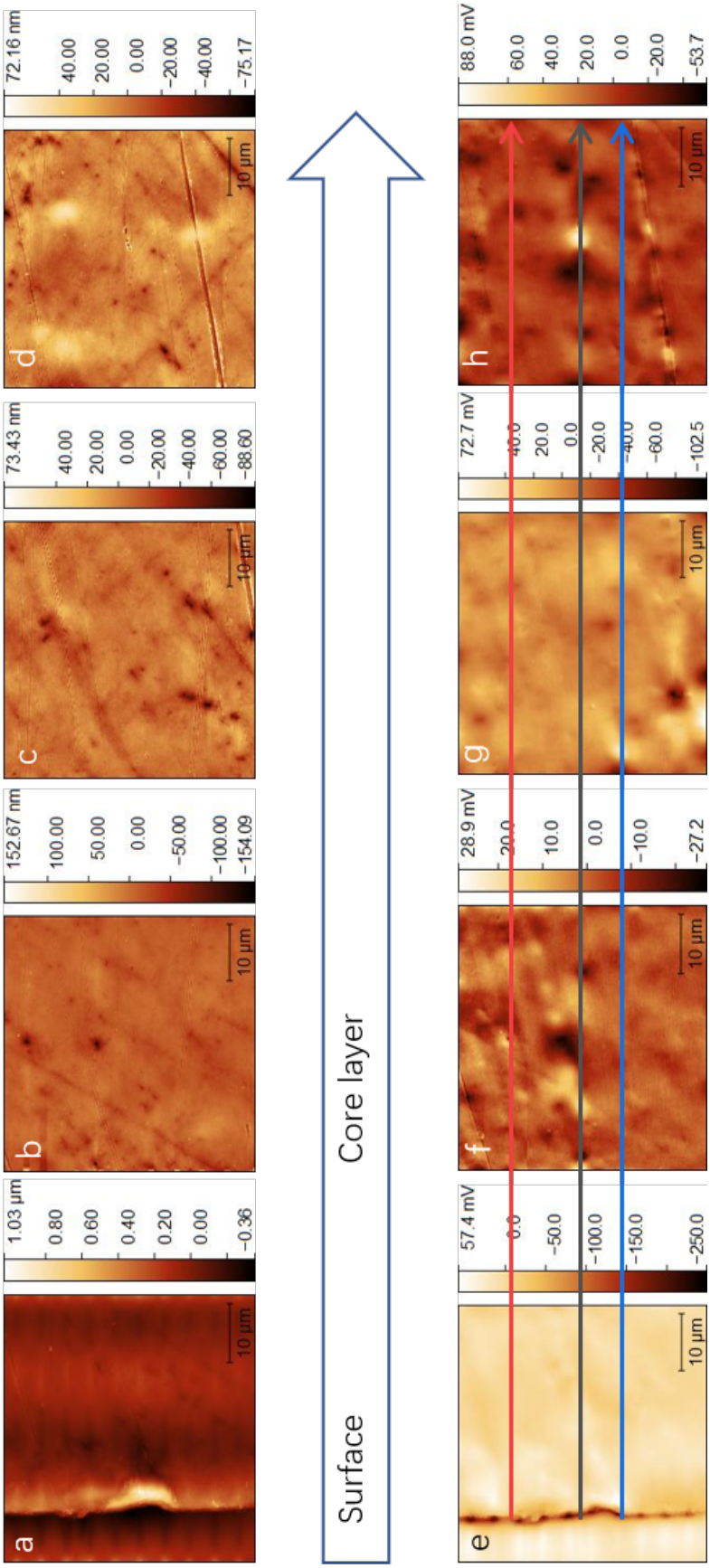

Figure 3.25: SKPFM result of alloy 8125: (a) to (d) are topography maps, (e) to (h) are Volta potential maps.

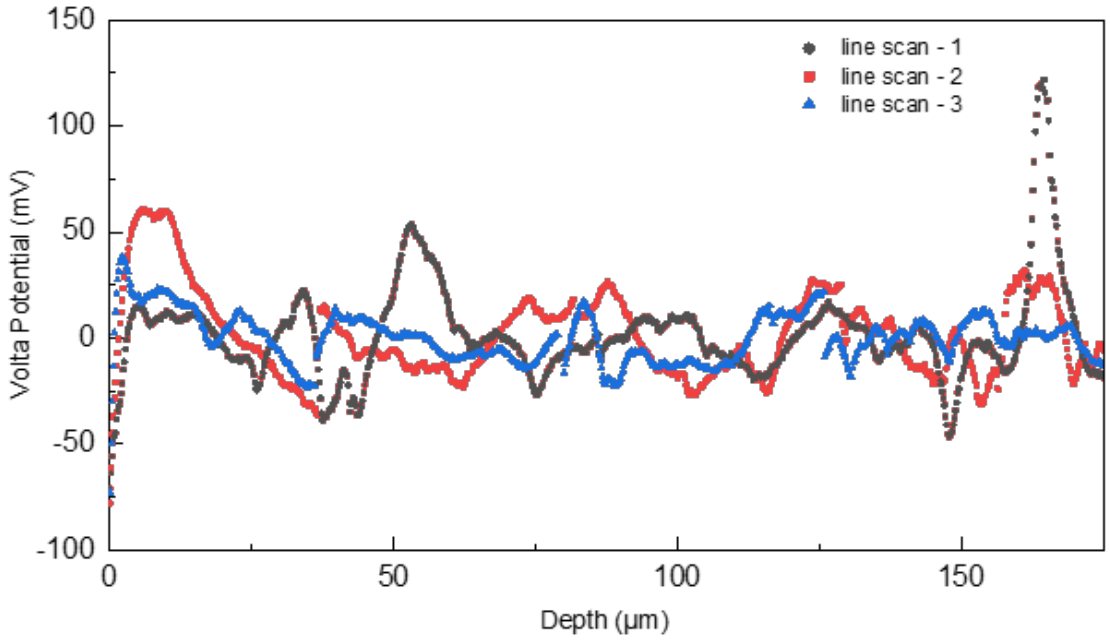

Figure 3.26: Volta potential variation through the cross-section of alloy 8125.

3.3 DISCUSSION

In the previous sections, the results of two types of samples FAB913 and 8125 obtained from the electrochemical measurements were displayed and analyzed, and the microstructural investigation was presented to guide and support the further understanding.

Combing the GDOES elemental profiling and the polarization results, in the case of sample-FAB913, the concentration of alloying elements are relatively low in the depth of 10 and 20 μm (corresponding to the heat affected zone and the diffusion zone) comparing to that in the other depths, so that the amount of intermetallic particles are much lower, leading to good corrosion resistance. The corrosion responses in these two depths are the least severe. The corrosion potential difference even reaches up to approximately 150 mV.

The result of OCP values, corrosion potentials, and corrosion current densities in each depth is integrated in Table 3.5. Figure 3.27a shows more intuitive. At the depth of 10 and 30 μm, there is a big difference between the OCP value and corrosion potential. The reason could be that the OCP value did not really reach a stable stage. It still had the potential to change after 15-min immersion, contributing to the result of mismatching.

In the depth of 30, 50, and 70 μm (core layer), the corrosion performance is lower than in HAZ and DZ. The dominant intermetallic particles in system FAB913 are Al(Fe,Mn)Si particles, which are cathodic particles. The increase of the Mn/Fe ratio can reduce the potential difference between matrix and intermetallic particles, which was proved by Zamin et al. [34] (they use Al alloy that is free of

Cu element). In system FAB913, the Mn/Fe ratio increases from HAZ to the core layer. The effect of Cu content was studied by Cao et al. They found that some Cu dissolved in the Al-matrix and the others incorporated in Al(Fe,Mn)Si particles. The addition of Cu strengthens the Al alloy, however, the incorporation of Cu in Al(Fe,Mn)Si particles leads to an increase of potential between the Al-matrix and the intermetallic particles [35]. Therefore, with the net effect of the presence of Cu and the increase of the Mn/Fe ratio, the potential difference between the intermetallic particles and the Al-matrix increased. Moreover, the corrosion current densities in these three depths are higher than in 10 and 20 μm. The increase of the Cu content from 20 μm to the core layer also rises the susceptibility of corrosion attack, contributing to a lower resistance performance.

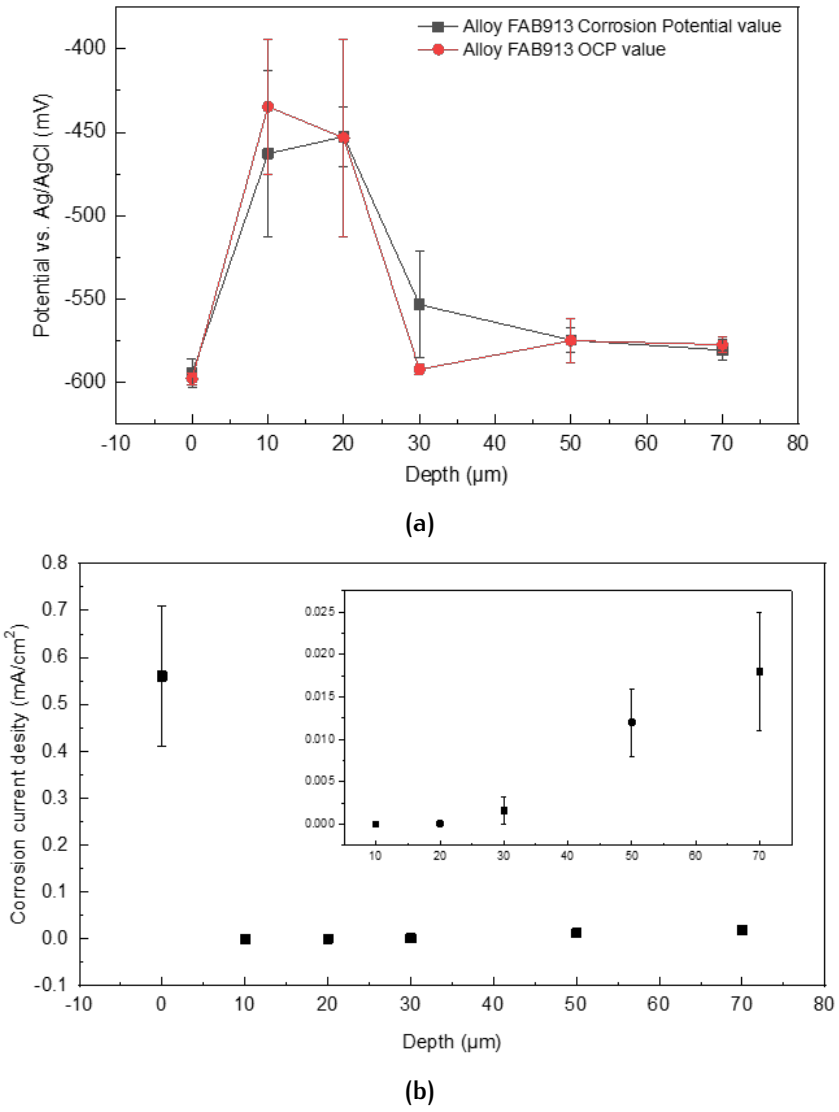

Figure 3.27: The electrochemical depth profiling of FAB913.

With regard to system - 8125, the electrochemical results show different corrosion responses than the other sample - FAB913. The integrated electrochemical results of 8125 and the electrochemical depth profiling are shown below in Table 3.6 and Figure 3.28a. The corrosion performance in the depth of 70 μm is the

Table 3.5: Electrochemical results of sample - FAB913.

Alloy FAB913	OCP value (mV)	Corrosion Potential (mV)	Corrosion Current Density (mA/cm^2)
Surface	-597.7±3.5	-594.4±8.4	$(5.6\pm1.5)x10^{-1}$
10 μm	-434.5±40.3	-462.8±50.1	$(1.8\pm1.2)x10^{-5}$
20 μm	-453.3±59.1	-452.5±17.65	$(6.5\pm0)x10^{-5}$
30 μm	-592.2±2.9	-553.3±31.8	$(1.6\pm1.6)x10^{-3}$
50 μm	-574.9±13.2	-574.6±7.5	$(1.2\pm0.4)x10^{-2}$
70 μm	-577.3±4.8	-580.5±6.0	$(1.8\pm0.7)x10^{-2}$

highest with both low corrosion current density and noble corrosion potential. According to the GDOES result, the Cu content is high (0.8 wt%) in this depth, which leads to an increase of the corrosion potential. Meanwhile, the concentration of Si is very low (0.05 wt%). The effect of Si in Al brazed material was studied by Afshar et al. He observed that the oxygen reduction current density at the Si particles is low so that Si particles would not be the active cathodic sites [10, 36]. However, he also proved that the presence of α-Al(Fe,Mn)Si particles increased the corrosion susceptibility. Therefore, an assumption could be made that the decrease of Si promotes corrosion performance due to less Si content in Al(Fe,Mn)Si particles, contributing to a lower corrosion current density. Same as in the sample - FAB913, in the depth of 10 and 20 μm, depletion of alloying elements results in good corrosion resistance. As for in the depth of 50 μm, the corrosion performance was not good as in the other depths although still better than at the surface. The reason for the different corrosion response could be the net effect of relatively high concentration of Cu and Si in this region. As mentioned above, Al(Fe,Mn)Si particles in Cu-containing alloy with a high Mn/Fe ratio have a harmful influence on the matrix. A large potential difference exists between the intermetallic particles and the matrix, which can easily form a galvanic cell to accelerate the corrosion.

Table 3.6: Electrochemical results of sample - 8125.

Alloy 8125	OCP Value (mV)	Corrosion Potential (mV)	Corrosion Current Density (mA/cm^2)
Surface	-585.7±7.0	-558.1±8.3	$(1.0\pm0.3)x10^{0}$
10 μm	-477.8±12.1	-474.3±35.5	$(2\pm2)x10^{-4}$
20 μm	-582.6±10.0	-488.6±17.9	$(1.6\pm0.9)x10^{-5}$
30 μm	-509.6±9.1	-520.9±1.6	$(4.9\pm0.5)x10^{-5}$
50 μm	-582.6±8.2	-554.6±7.0	$(1.3\pm1.2)x10^{-1}$
70 μm	-471.0±41.1	-295.7±8.9	$(3.4\pm1.1)x10^{-5}$

When comparing two types of systems, it is worth mentioning that in system - FAB913, the corrosion performance in the HAZ and DZ is the best while in system - 8125, the deep core layer shows better performance than in the HAZ and DZ. Overall, the presence of HAZ and DZ effectively protects the core layer of the aluminium brazing sheet.

Figure 3.29 shows the morphology of two samples in the depth of 10 μm. In

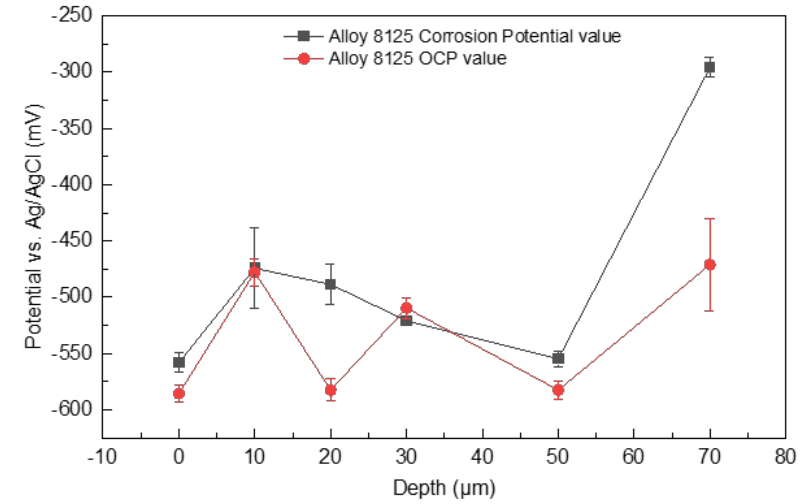

(a)

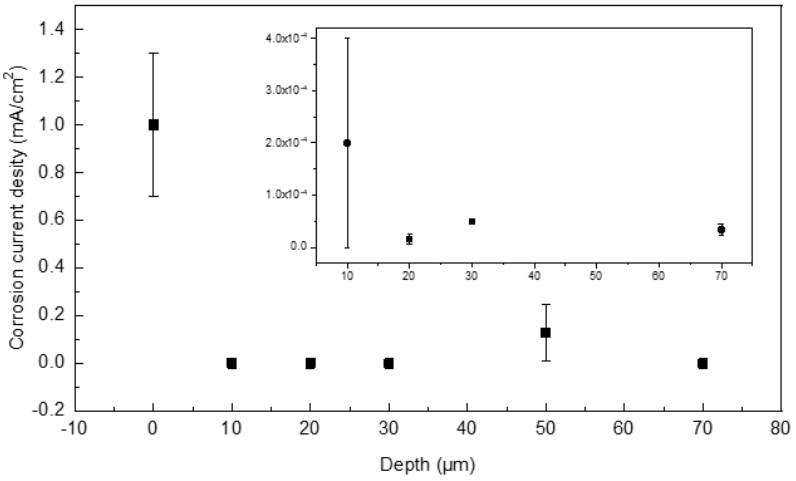

(b)

Figure 3.28: The electrochemical depth profiling of alloy 8125.

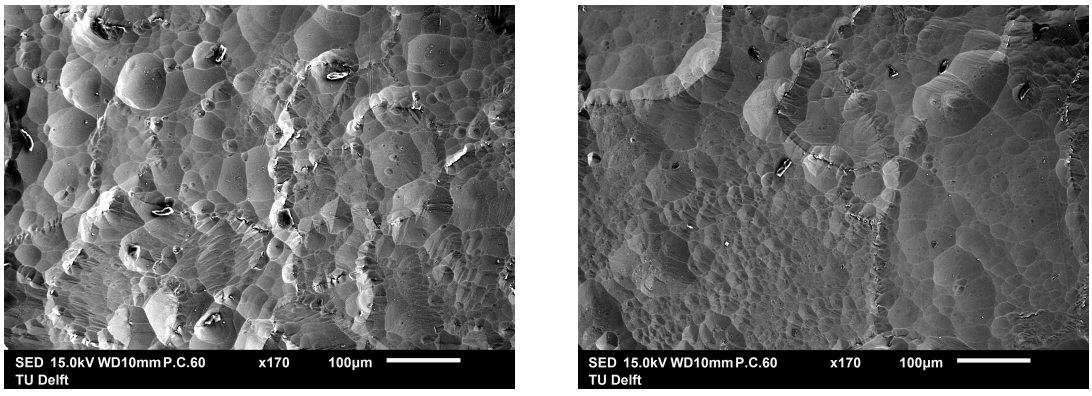

(a) (b)

Figure 3.29: SEM images in the depth of 10 μm with 170x magnification of (a) sample - FAB913 and (b) sample - 8125.

both systems, it is located at the HAZ or the interface between HAZ and DZ. The amount of intermetallic particles is limited in this region. And the particles were detected preferentially embedded at the grain boundary. It has been studied that the dominant corrosion mechanism in the aluminium brazing sheet is IGC. The corrosion commonly starts at the surface. After the damage exists at the surface, the corrosion penetrates towards to the core layer along the grain boundary. At the end, the material was failure in the form of IGC and local pitting [14]. The nature shown in the figure explains the reason for the occurrence of IGC to some extent. Most of the intermetallic particles in these two systems behave as cathodes. The matrix around the particles would get corroded first due to the high potential difference. Now the particles are mostly located at the grain boundaries. This feature makes this HAZ and DZ more sensitive to IGC, finally contributing to the existence or acceleration of IGC.

As for the correlation between SKPFM result and electrochemical result. Both of them indicate two same features. The first is at the re-solidified clad layer, the surface had a very high reaction activity, can easily get severe corrosion attack (verified by Figure 3.9b, Figure 3.10, Figure 3.22, and Figure 3.23). In the Volta potential map, the Volta potential value at the surface is approximately 50 mV lower than the average number of the core layer, which means the surface is preferentially dissolved when corrosion occurs. The other co-verified fact is that the HAZ and DZ are relatively nobler than the other layers, especially comparing to the surface. The Volta potential difference between the HAZ and surface can reach up to 125 mV. The reason for the two different values of Volta potential difference between the surface and the core layer in the two systems could be the different concentrations of the Cu element. As mentioned above, the addition of Cu elements increases the potential difference between the matrix and the intermetallic particles. The Cu content in the core layer of system 8125 is higher than in the core layer of system FAB913. More Cu diffused into the re-solidified clad layer during brazing process in system 8125. Therefore, the Volta potential difference between the surface and the core layer is larger in system 8125.

4 CONCLUSION

Corrosion properties in different depths of aluminium brazing sheets FAB913 and 8125 are investigated in this thesis. Electrochemical measurements include open circuit potential measurement and potentiodynamic polarization test, which were utilized to study the corrosion performance in the environment, including Cl^- ion and hydrogen peroxide. Optical microscope and scanning electron microscope were used to investigate the microstructural evolution after polarization. Besides, a material characterization technology widely used in aluminium alloy study - scanning Kelvin probe force microscope was implemented to visualize the Volta potential variation through the cross-section.

According to the results, the heat affect area and diffusion zone generated during the brazing process show good corrosion performance while severe corrosion attacks can easily happen at the surface of the re-solidified clad layer. The amount of intermetallic particles in these two regions is low. The existence of HAZ and DZ protects the core layer to some extent. Combing with GDOES depth profiling, the amount of Cu and Si element and the Mn/Fe ratio are the main impact factors influence the corrosion performance.

Although experiment methods are limited and difficult to be conducted in the GDOES sputtering craters, samples with different depths gave the possibility to investigate the corrosion behavior and microstructural evolution in each distinguished region, which contributes to more extensive information with the combination of the study at the cross-section.

It is not easy to compare the Volta potential maps gained from SKPFM with the polarization results. The conclusion that can be drawn is that the Volta potential at the surface is relatively low which explains the revealed high reaction activity. Meanwhile, the Volta potential is relatively high at the HAZ and DZ that accounts for good corrosion performance. Intermetallic particles existing in system FAB913 and 8125 mostly have much higher Volta potential than the matrix, which means they would act as a cathode during corrosion.

5 RECOMMENDATION

Based on the results and discussion in this thesis, further research could be carried out as follows:

1. 0.05 M NaCl solution with 0.1 ml/L H_2O_2 was used as the electrolyte during the electrochemical experiments. The change of the microstructure is not very evident under the optical and SEM observation. It is possible to increase the concentration of NaCl solution to make the microstructural evolution more obvious.

2. The corrosion performance of two systems in the polarization experiments has been studied. The life-time of two systems could be further investigated by immersion test.

3. The sample set-up was hand-made, it is convenient, however, electrolyte leakage could potentially happen under the tape which was used to cover the rest of the surface. It would be better to use a pipette tip to set a micro-electrochemical cell to re-run the experiments to check the results.

4. The Mn/Fe ratio is known as the impact factor that can influence the corrosion performance. In further research, how the Mn/Fe ratio affects the corrosion behavior could be investigated.

5. The SKPFM measurement was processed in the normal open air environment, which is different from the more aggressive environment in which electrochemical experiments were conducted (containing chloride irons and hydrogen peroxide). The obtained Volta potential analysis result may misconstrue the true corrosion nature. In future work, there could be two better methods: 1) perform the SKPFM experiments under a controlled environment with humidity and temperature; 2) perform the SKPFM experiments before and after polarization in NaCl solution. Then the real nature of corrosion under different environment can be studied, from which the corrosion mechanism could also be explained.

6 BIBLIOGRAPHY

[1] P. Mukhopadhyay, "Alloy designation, processing, and use of aa6xxx series aluminium alloys," *ISRN Metallurgy*, vol. 2012, 2012.

[2] W. Hufnagel, *Key to Aluminium Alloys: Aluminium-Schlüssel*. Aluminium-Verlag, 1991.

[3] J. Lacaze, S. Tierce, M.-C. Lafont, Y. Thébault, N. Pébère, G. Mankowski, C. Blanc, H. Robidou, D. Vaumousse, and D. Daloz, "Study of the microstructure resulting from brazed aluminium materials used in heat exchangers," *Materials Science and Engineering: A*, vol. 413, pp. 317–321, 2005.

[4] J. R. Davis, *Alloying: understanding the basics*. ASM international, 2001.

[5] R. Elliott, *Cast iron technology*. Butterworth-Heinemann, 1988.

[6] J. Mattheij, "Role of brazing in repair of superalloy components–advantages and limitations," *Materials science and technology*, vol. 1, no. 8, pp. 608–612, 1985.

[7] F. N. Afshar, J. De Wit, H. Terryn, and J. Mol, "Scanning kelvin probe force microscopy as a means of predicting the electrochemical characteristics of the surface of a modified aa4xxx/aa3xxx (al alloys) brazing sheet," *Electrochimica acta*, vol. 88, pp. 330–339, 2013.

[8] A. J. Wittebrood, "Microstructural changes in brazing sheet due to solid-liquid interaction," 2009.

[9] D. Schnee, "Principles of brazing and soldering." Brochure, 2019.

[10] F. N. Afshar, J. De Wit, H. Terryn, and J. Mol, "The effect of brazing process on microstructure evolution and corrosion performance of a modified aa4xxx/aa3xxx brazing sheet," *Corrosion science*, vol. 58, pp. 242–250, 2012.

[11] F. N. Afshar, A. Glenn, J. De Wit, H. Terryn, and J. Mol, "A combined electron probe micro analysis and scanning kelvin probe force microscopy study of a modified aa4xxx/aa3xxx aluminium brazing sheet," *Electrochimica Acta*, vol. 104, pp. 48–63, 2013.

[12] D. Schmatz, "Grain boundary penetration during brazing of aluminum," *Welding Journal*, vol. 62, no. 10, pp. 267–271, 1983.

[13] Z. Yuan, F. Tao, J. Wen, and Y. Tu, "The dependence of microstructural evolution and corrosion resistance of a sandwich multi-layers brazing sheets on the homogenization annealing," *IEEE Access*, vol. 7, pp. 121388–121394, 2019.

[14] W. Liu, Z. Yang, L. Li, and D. Zhou, "An investigation on corrosion behavior of a multi-layer modified aluminum brazing sheet," in *MATEC Web of Conferences*, vol. 61, p. 05003, EDP Sciences, 2016.

[15] A. Turnbull, "Modelling of environment assisted cracking," *Corrosion science*, vol. 34, no. 6, pp. 921–960, 1993.

[16] I. Huang and W. Evan, *Uniform Corrosion and General Dissolution of Aluminum Alloys 2024-T3, 6061-T6, and 7075-T6*. PhD thesis, The Ohio State University, 2016.

[17] K. Schäuble, *Silica passivation layer on aluminium brazing sheets*. PhD thesis, Universität zu Köln, 2010.

[18] A. S. H. Makhlouf, V. Herrera, and E. Muñoz, "Corrosion and protection of the metallic structures in the petroleum industry due to corrosion and the techniques for protection," in *Handbook of Materials Failure Analysis*, pp. 107–122, Elsevier, 2018.

[19] C. Vargel, *Corrosion of aluminium*. Elsevier, 2020.

[20] G. Frankel, "Pitting corrosion of metals a review of the critical factors," *Journal of the Electrochemical Society*, vol. 145, no. 6, pp. 2186–2198, 1998.

[21] N. Birbilis and B. Hinton, "Corrosion and corrosion protection of aluminium," in *Fundamentals of Aluminium Metallurgy*, pp. 574–604, Elsevier, 2011.

[22] H. Leckie and H. Uhlig, "Environmental factors affecting the critical potential for pitting in 18–8 stainless steel," *Journal of the Electrochemical Society*, vol. 113, no. 12, pp. 1262–1267, 1966.

[23] V. Sinyavskii, V. Ulanova, and V. Kalinin, "On the mechanism of intergranular corrosion of aluminum alloys," *Protection of metals*, vol. 40, no. 5, pp. 481–490, 2004.

[24] J. I. Goldstein, D. E. Newbury, J. R. Michael, N. W. Ritchie, J. H. J. Scott, and D. C. Joy, *Scanning electron microscopy and X-ray microanalysis*. Springer, 2017.

[25] D. G. Enos, "The potentiodynamic polarization scan," tech. rep., Department of Materials Science and Engineering, University of Virginia, 1997.

[26] B. N. Popov, *Corrosion engineering: principles and solved problems*. Elsevier, 2015.

[27] A. Berradja, "Electrochemical techniques for corrosion and tribocorrosion monitoring: Methods for the assessment of corrosion rates," in *Corrosion Inhibitors*, IntechOpen, 2019.

[28] X. Chen, W. Tian, S. Li, M. Yu, and J. Liu, "Effect of temperature on corrosion behavior of 3003 aluminum alloy in ethylene glycol–water solution," *Chinese Journal of Aeronautics*, vol. 29, no. 4, pp. 1142–1150, 2016.

[29] P. Schmutz and G. Frankel, "Corrosion study of aa2024-t3 by scanning kelvin probe force microscopy and in situ atomic force microscopy scratching," *Journal of the Electrochemical Society*, vol. 145, no. 7, p. 2295, 1998.

[30] C. Örnek, C. Leygraf, and J. Pan, "On the volta potential measured by skpfm–fundamental and practical aspects with relevance to corrosion science," *Corrosion Engineering, Science and Technology*, vol. 54, no. 3, pp. 185–198, 2019.

[31] T. Muster and A. Hughes, "Applications and limitations of scanning kelvin probe force microscopy for the surface analysis of aluminum alloys," *Journal of The Electrochemical Society*, vol. 153, no. 11, pp. B474–B485, 2006.

[32] A. J. Wittebrood, "Microstructural changes in brazing sheet due to solid-liquid interaction," 2009.

[33] F. N. Afshar, "Enhanced corrosion protection by microstructural control of aluminium brazing sheet," 2013.

[34] M. Zamin, "The role of mn in the corrosion behavior of al-mn alloys," *Corrosion*, vol. 37, no. 11, pp. 627–632, 1981.

[35] C. Cao, D. Chen, X. Fang, J. Ren, J. Shen, L. Meng, J. Liu, L. Qiu, and Y. Fang, "Effects of cu addition on the microstructure and properties of the al–mn–fe–si alloy," *Journal of Alloys and Compounds*, p. 155175, 2020.

[36] F. N. Afshar, R. Ambat, C. Kwakernaak, J. De Wit, J. Mol, and H. Terryn, "Electrochemical depth profiling of multilayer metallic structures: An aluminum brazing sheet," *Electrochimica acta*, vol. 77, pp. 285–293, 2012.

A APPENDIX

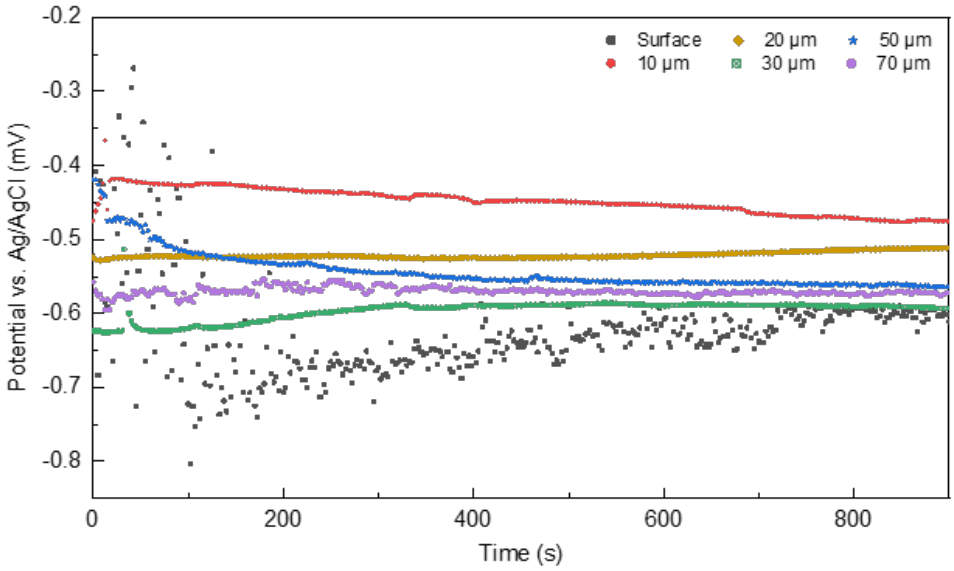

Figure A.1: OCP curves of sample - FAB913 at different depths in 0.05 M NaCl solution with 0.5 ml/L H_2O_2.

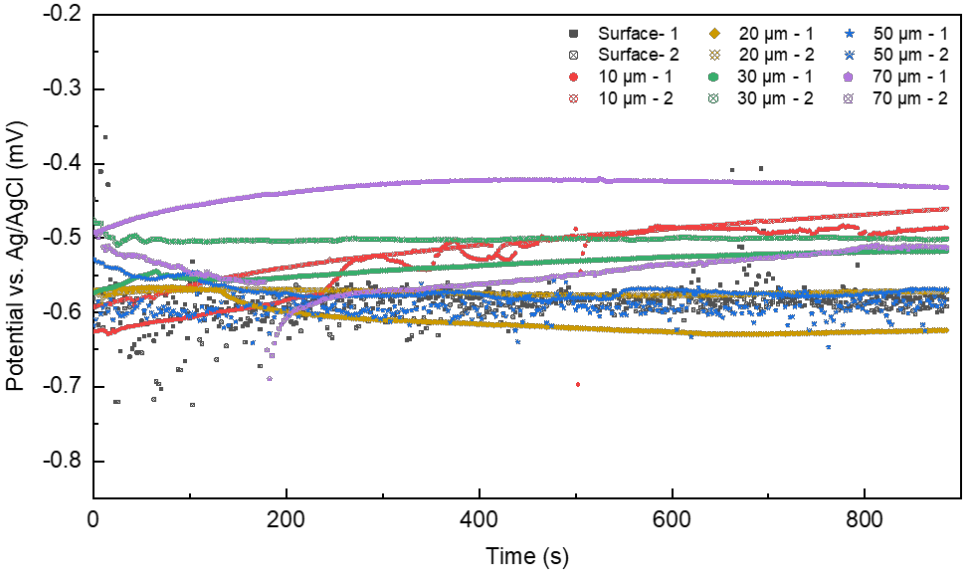

Figure A.2: OCP curves of sample - 8125 at different depths in 0.05 M NaCl solution with 0.5 ml/L H_2O_2.

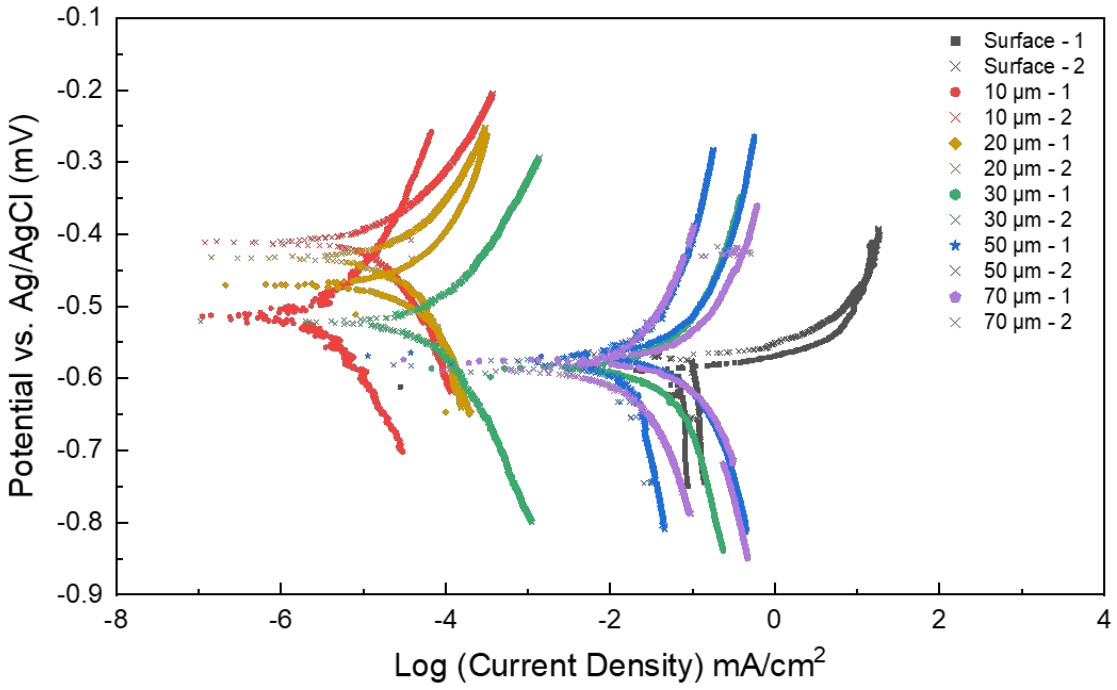

Figure A.3: Polarization curves of sample - FAB913 at different depths in 0.05 M NaCl solution with 0.5 ml/L H_2O_2.

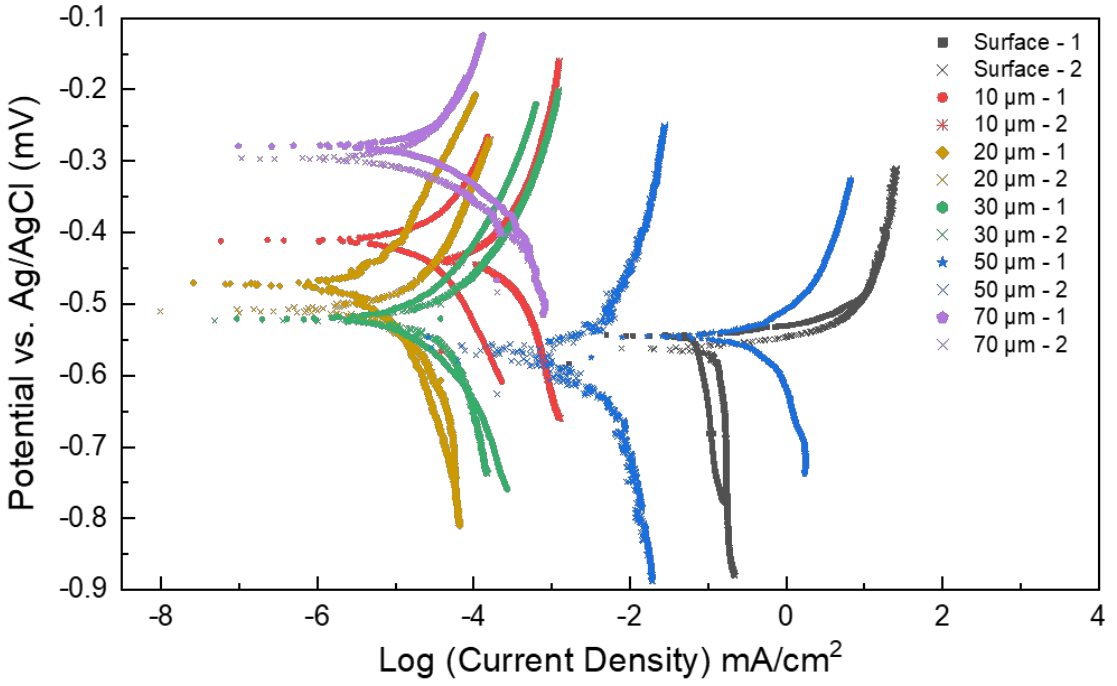

Figure A.4: Polarization curves of sample - 8125 at different depths in 0.05 M NaCl solution with 0.5 ml/L H_2O_2.

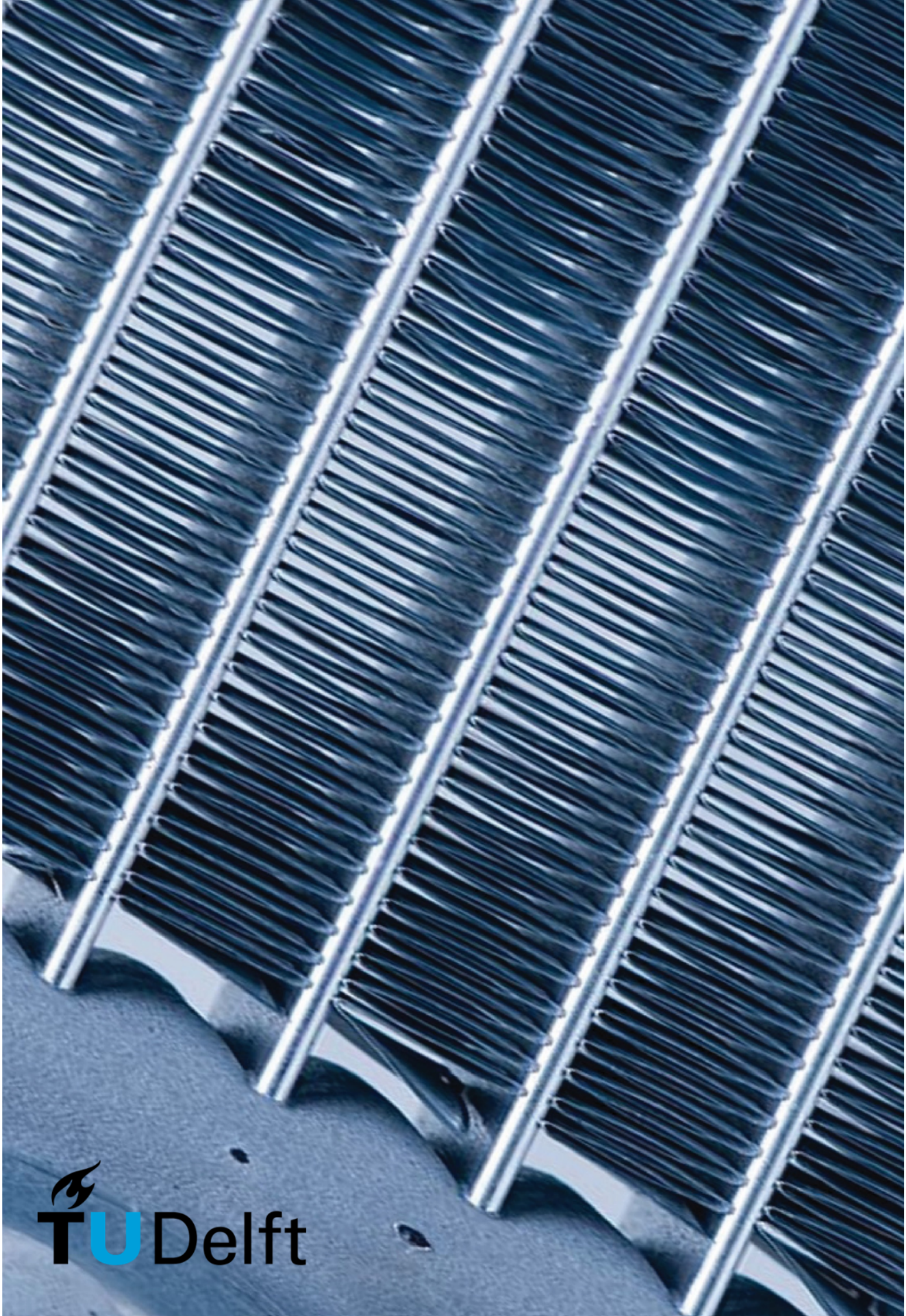
TU Delft